# Study on the Ocean Colour Fluorescence Product

ATBD

---

---

*Date:*
June 19, 2020

*Prepared by:*
Lena Kritten


| Document Version | Date | Changes | Originator |
|---|---|---|---|
| ATBD v1.0 | 25.04.2019 | | Lena Kritten |
| ATBD v1.1 | 02.09.2019 | | Lena Kritten |
| ATBD v1.2 | 07.01.2020 | | Lena Kritten |
| ATBD v1.3 | 17.03.2020 | | Lena Kritten |
| ATBD v1.4 | 19.06.2020 | | Lena Kritten |

Table 1: Version History

Table 2: Acronyms and Abbreviations

| | |
|---|---|
| $L_w$ | water-leaving radiance |
| $nL_w$ | normalized water-leaving radiance |
| $R_{rs}$ | remote-sensing-reflectance |
| $F_0$ | extraterrestrial solar irradiance at mean Earth-Sun distance, seasonally corrected |
| $[\rho_w]_N$ | normalized water-leaving reflectance |
| RTM | Radiative Transfer Model |
| RT | Radiative Transfer |
| L-FPH | Fluorescence Peak Height based on TOA radiance |
| $\rho_w$-FPH | Fluorescence Peak Height based on water-leaving reflectance |
| BRDF | Bidirectional Reflectance Distribution Function |
| $\theta_S$ | solar zenith angle |
| $\theta_V$ | viewing zenith angle |
| $\phi_V$ | viewing azimuth angle |
| srf | spectral response function |
| Chl | chlorophyll concentration |

# Contents

# 1 Introduction

We investigated and developed a new Ocean Colour Fluorescence Product in the framework of EUMETSAT's initiative to improve and to develop new products for Sentinel-3 OLCI observation and implemented a product validation and review process. We aim to deliver an advanced and robust algorithm, that uses OLCI spectral capabilities and ensures a high quality Fluorescence retrieval meeting user requirements in open ocean and complex waters. Phytoplankton absorb sun light and use this energy through photosynthesis to produce organic material. Chlorophylls, present in all phytoplankton cells, induce two dominant peaks in absorption spectra, the primary in the blue (440 nm) and the secondary in the red part of the spectrum (675 nm). Phytoplankton also dissipate a fraction around 0.03 Zhou et al. (2008) of the absorbed solar energy through Fluorescence which generates a radiance peak around the wavelength of 681 nm. The concept of this new and proposed fluorescence algorithm is to limit the analysis range to the red part of the spectrum and to approximate the phytoplankton fluorescence peak and the secondary absorption peak with two Gaussian functions, while all other absorption and scattering processes are captured by a slope and an offset.

## 1.1 Product Description

The OC-Fluo algorithm delivers different products. Each is described separately here. The main products delivered from this study are L-FPH, if Level1 data is processed, and $\rho_w$-FPH, if Level2 data is processed.

### 1.1.1 Radiance Fluorescence Peak Height (L-FPH)

L-FPH is the amplitude of the Gaussian function, which is related to the fluorescence peak (centered at 682.5 nm) that is fitted to Level-1 radiance ($L_{TOA}$). It is therefore a measure of the fluorescence signal in the TOA radiance spectrum without any normalization. L-FPH is given in units of $Wm^{-2}sr^{-1}nm^{-1}$.

### 1.1.2 Water-leaving-reflectance Fluorescence Peak Height ($\rho_w$-FPH)

$\rho_w$-FPH is the amplitude of the Gaussian function, which is related to the fluorescence peak (centered at 682.5 nm) that is fitted to Level-2 water-leaving reflectance ($\rho_w$). It is a measure of the fluorescence signal in the water-leaving reflectance which is dimensionless and therefore $\rho_w$-FPH is dimensionless. Operational OLCI L2 products are defined as the directional water-leaving reflectance. The OLCI L2 products include the corrections to the water reflectance value with the Sun at zenith, the mean Earth-Sun distance, and non-attenuating atmosphere. They do not include the BRDF corrections for viewing geometry, water optical properties, and the sky radiance distribution.

### 1.1.3 Radiance Absorption Peak Depth (L-APD)

L-APD is the amplitude of the Gaussian function, which is related to the absorption dip that is fitted to Level-1 radiance. It is therefore a measure of the absorption signal in the TOA radiance spectrum without any normalization. L-APD is given in units of $Wm^{-2}sr^{-1}nm^{-1}$. This product is

for this study a by-product and not validated.

### 1.1.4 Water-leaving-reflectance Absorption Peak Depth ($\rho_w$-APD)

$\rho_w$-APD is the amplitude of the Gaussian function, which is related to the absorption dip that is fitted to Level-2 water-leaving reflectance ($\rho_w$). It is therefore a measure of the absorption signal in the remote-sensing reflectance which is normalized by irradiance. $\rho_w$-APD is dimensionless. This product is for this study a by-product and not validated.

| Input | Bands | Processing Level | Description | Output | Description | Unit |
|---|---|---|---|---|---|---|
| $L_{TOA}$ | Oa08- Oa12 | Level-1B | Spectral top- of-atmosphere radiance | L-FPH / L-APD | radiance Fluorescence Peak Height / radiance absorption peak depth | $mWm^{-2}sr^{-1}nm^{-1}$ |
| $\rho_w$ | Oa08- Oa12 | Level-2 | water-leaving reflectance/ Surface directional r eflectance, corrected for atmospheric attenuation, the Sun illumination geometry, and the mean Earth-Sun distance. | $\rho_w$-FPH / $\rho_w$-APD | water-leaving reflectance Fluorescence Peak Height / water-leaving reflectance absorption peak depth | - |

Table 3: In- and output description of the OC-Fluo algorithm.

### 1.1.5 Normalization

Fluorescence products are customarily given in the unit of the processed quantity, because they measure the height or amplitude of the fluorescence peak in the measured spectrum. In order to put our fluorescence products in relation to the well-established normalized fluorescence line height (nFLH) of MODIS, we give here the corresponding equations. There are a number of steps in the normalization of water reflectances. The MODIS fluorescence algorithm returns nFLH in $mW\,cm^{-2}\mu m^{-1}\,sr^{-1}$, calculated as the difference between the observed normalized water-leaving radiance at 678 nm (nLw(678)) and a linearly interpolated nLw(678) from two surrounding bands (Behrenfeld et al., 2009). The normalized water-leaving radiance is fully normalized, including the BRDF correction. The relation between nLw and $\rho_w$ is the following (Gordon and Voss, 1999):

$$[\rho_w]_N = \frac{\pi}{F_0}[L_w]_N = \frac{R/R_0 * \rho_w}{cos(\theta_S) * t(\theta_S)} \quad (1)$$

Where $\theta_S, \theta_V$ and $\phi$ are the sun zenith angle, the viewing zenith angle and the azimuth angle respectively. While $\rho_w(\theta_S, \theta_V, \phi)$ can have different values for each combination of angles, $\rho^{NW}$ is per definition $\rho_w$ at $\theta_S = 0$ and $\theta_V = 0$.

The presented $\rho_w$-FPH is based on OLCI's $\rho_w$, which includes the correction to the Sun at zenith, the mean Earth-Sun distance, and non-attenuating atmosphere. It does not include the BRDF correction for viewing geometry, water optical properties, and the sky radiance distribution. The normalization by $F_0$ also removes interfering spectral features of the solar radiation, so that they are not mixed up with the desired fluorescence features.

The presented L-FPH is based on $L_{TOA}$, which does not include any of the before-mentioned corrections, but the preprocessing of the retrieval of L-FPH includes the normalization to the mean solar irradiance $F_0$ (see Sect. 3.5).

## 1.2 Product Requirements

The Sentinel-3 mission has no requirements directly addressing the chlorophyll fluorescence signal accuracy, however, chlorophyll concentration and associated error estimates in coastal and open ocean waters is one of the core products to be produced (Craig Donlon, 2011). We therefore base our requirements of the fluorescence product on requirements of chlorophyll concentration and adapt them to requirements of fluorescence, once we have retrieved a functional relation. The following requirements on chlorophyll concentration and relevant measures for our retrieval are adapted from Drinkwater and Rebhan (2005).

Table 4: Geophysical parameters and accuracies for Ocean Colour (under clear daytime conditions) adapted from (Drinkwater and Rebhan (2005))

| Parameter | Range | Accuracy Case 1 water | Accuracy Case 2 water |
|---|---|---|---|
| Marine Reflectance [at 442 nm] | 0.001 - 0.04 | 5 x 10-4 | 5 x 10-4 |
| Water leaving radiance Lw (λ) (atmospherically corrected) [mW/cm2/µm/Sr] | 0.0 - 1.0 | 5% | 5% |
| Photosynthetically available radiation, PAR [µmol quanta/m²/s] | 0 - 1400 | 5% | 5% |
| Chlorophyll, Chl [mg/m³] | 0.001 - 150 | threshold 30%, goal 10% | threshold 70%, goal 10% |

Additionally we express qualitative requirements on the product:

- The product $F_w$ shall be a measure of the water-leaving fluorescence signal, without disturbance from other optically active substances.
- $F_w$ should be sensitive to chlorophyll concentration
- The product should not be sensitive to atmospheric effects

- Chlorophyll Fluorescence is linked to the chlorophyll concentration, phytoplankton physiology and a variety of other factors and the relationship is complex, which will be described in the next section. It is dominated by a positive correlation with saturation of fluorescence at high concentration values, which is caused by chlorophyll pigment packaging. We will aim for the release of an average functional relationship between the fluorescence and the concentration in order to translate the fluorescence product into chlorophyll concentration if required.

The interpretation of the fluorescence signal has to take photoinhibition, phytoplankton species, and physiological states into account.

## 1.3 Scientific state-of-the-art

Chlorophyll fluorescence is light re-emitted by chlorophyll molecules when returning from excited to non-excited states. Quantification of solar-induced phytoplankton fluorescence has two main advantages in marine bio-geochemistry applications (Craig Donlon (2011); Donlon et al. (2012)). These are, 1) the improvement of the chlorophyll retrieval, which is customarily based on the detection of the chlorophyll absorption signal (Odermatt et al. (2012); Xing et al. (2007); Neville and Gower (2008)). Remotely sensed Fluorescence Line Height (FLH, see also eq.
2) can better reveal blooms in coastal areas than surface chlorophyll based on the ratios of water-leaving radiances in the blue and green spectral range (440-560 nm) by allowing better differentiation of phytoplankton chlorophyll-a concentrations from suspended sediments and yellow matter (Gower and King (2012)). 2) additional information on phytoplankton physiological state, biomass and maximum layer depth can be gained through the ratio of the chlorophyll fluorescence to absorption signal (Babin et al. (1996)).

The pure fluorescence signal does not only vary with variation in the chlorophyll-a pigment concentration, but is also affected by photoinhibition, phytoplankton species, and physiological states (Falkowski and Kiefer (1985); Mazeran et al. (2017)), and layering of phytoplankton. Borstad et al. (1987) compiled fluorescence observations from several years and found that the relationship between FLH and chlorophyll could vary by a factor of eight. They also noted that the correlation within a particular study region was quite good and that the large variability only occurred when comparing different studies. In general, the reported fluorescence signal varies from 0.01 to 0.08 W/m2/sr/mm per mg Chl. Lin et al. (2016) reports a strong diel cycle in in-situ measured fluorescence lifetime (which has a strong positive correlation to fluorescence efficiency), where the efficiency (lifetime) is higher at night than during daytime in spite of a marked increase under strong sunlight.

One of the major design goals of the Medium Resolution Imaging Spectrometer (MERIS) was the capability to use the signal from chlorophyll fluorescence stimulated by ambient sunlight to detect and map phytoplankton. The use of chlorophyll fluorescence was considered to be especially useful in coastal waters. Based on a variety of studies, the three spectral channels centred at 665, 681.25 and 705 nm were included in the design of MERIS for retrieving the fluorescence signal.

Using RTM, Fischer and Kronfeld (1990) stated the sun-stimulated natural fluorescence of chlorophyll-a a good predictor for phytoplankton, even in optically complex waters with varying suspended matter and yellow substance concentrations. They found an increase in fluorescence of about 0.05 $Wm^{-2}sr^{-1}\mu m^{-1}$ caused by an increase in chlorophyll concentration of

1 mgm$^{-3}$, when a fluorescence efficiency factor of 0.3% was assumed. They also quantified the effect of vertical stratification.

As of now, the most established fluorescence product, which is operationally available is the Fluorescence Line Height (FLH) (Behrenfeld et al. (2009); Gower and King (2007a,b)). There, a baseline is first formed by a linear interpolation of two baseline bands, and then subtracted from the radiance of the fluorescence band to obtain the FLH. The equation reads:

$$FLH = L_F - [L_R + (\lambda_R - \lambda_F)/(\lambda_R - \lambda_L)(L_L - L_R)] \quad (2)$$

where $\lambda_F$, $\lambda_L$, $\lambda_R$ are the center wavelengths of the fluorescence band and the two baseline bands. $L_F$, $L_L$, $L_R$ are the radiances of the fluorescence band and the two baseline bands. For MERIS, the common band combination is $\lambda_F = 681$ nm, $\lambda_L = 665$ nm, $\lambda_R = 709$ nm. For MODIS, it is $\lambda_F = 678$ nm, $\lambda_L = 667$ nm, $\lambda_R = 748$ nm. For MODIS, the standard algorithm returns the normalized Fluorescence Line Height (nFLH) in mW cm$^{-2}$ µm$^{-1}$ sr$^{-1}$, calculated as the difference between the observed nLw(678) and a linearly interpolated nLw(678) from two surrounding bands. Here, normalization implies the application of a Bidirectional Reflectance Distribution Function (BRDF) correction. However, Gower (2014) concludes that normalization results in errors which make the fluorescence data much less useful and demonstrates that FLH should be used as a measure of chlorophyll concentration without normalization. Alternative algorithms use a simple reflectance ratio of the reflectance peak around 682 nm, e.g. reflectance at 670 and 560 nm Xing et al. (2007).

A number of studies investigated the performance of FLH compared to Chl abs in different regions. Hoge et al. (2003) conducted a validation of Terra-MODIS FLH using airborne laser-induced phytoplankton chlorophyll fluorescence data retrievals within Gulf Stream, continental slope, shelf, and coastal waters of the western North Atlantic Ocean. They derived a correlation coefficient of $r^2 = 0.85$ and conclude that the FLH is equally valid within similar oceanic provinces of the global oceans. Huot et al. (2005) discuss important sources of variability in sun-induced chlorophyll fluorescence, such as incident radiance, species composition and nutritional status, and examine difficulties in deriving fluorescence data products from satellite imagery. According to their findings MODIS FLH can be related to the total flux being emitted by fluorescence. Moreno-Madriñán and Fischer (2013) investigated the performance of the MODIS FLH algorithm in estuarine waters and derived no overall relationships between in-situ chlorophyll-a and the FLH product ($r^2$=0.20,n=507). Nevertheless, the obtained weak relationship was still eight times stronger than that between in-situ chlorophyll-a and the standard product OC3M traditionally used to estimate chlorophyll-a in ocean waters.

In the OLCI matchup protocol, the criteria for validation are described (EUMETSAT, 2019).

Gower and King (2007a) validated FLH from MERIS on the west coast of Canada. They present an average relation between FLH and surface chlorophyll concentration from research cruises and from the blue to green ratio observed by MERIS based on a simple model accounting for absorption of stimulating and emitted radiation by chlorophyll pigments, which gives a good fit to the observations. Their results show a difference between the FLH-chlorophyll-relation for offshore waters and those in coastal straits and inlets, which is in agreement with the findings of Gons et al. (2008), who documented the effective use of the MERIS FLH product in oligotrophic waters of the Laurentian Great Lakes, but failure (with FLH diminishing and becoming negative) in mesotrophic and eutrophic waters. Overall, we can assume that operational FLH algorithms that are based on the measurements of reflectance at three wavelengths in and around the fluorescence band, are sufficient for fluorescence retrieval in the open ocean where

atmospheric correction algorithms work well and elastic reflectance in the fluorescence band is well approximated by the baseline curve due to the relatively weak elastic scattering signal which depends on chlorophyll alone (Letelier (1996)). However, this is not the case in coastal areas. FLH prod- ucts in coastal waters are significantly affected by a peak in the underlying elastic reflectance which spectrally overlaps and contaminates any fluorescence retrieval (see figure 5 for visu- alization). The shape and magnitude of this near-infrared peak is the result of a modulation of the particulate elastic spectrum (from both algal and non algal particles) by the combined phytoplankton and water absorption spectra. The confluence of the decreasing phytoplankton absorption and the increasing absorption of water with wavelength results in a local absorption minimum. This absorption minimum leads to the maximum in the reflectance spectra which are inversely related to the total absorption.

Binding et al. (2011) even reported a moderate negative relationship ($R^2 = 0.57$) between FLH and in-situ chlorophyll at Lake of the Woods with chlorophyll concentration ranging between 2 - 70 $mg/m^3$. As a reason they suggested that at this intensity of a bloom the absorption signal of chlorophyll dominates in the 681 nm band leading to a negative FLH. Consequently, Ioannou et al. (2009) conclude that in order to improve the operational FLH algorithms for coastal waters and compensate for the effects of the overlap of fluorescence and elastic spectra, suitable models must be developed. Such models can take the larger impact of the spectral variation of the underlying elastic reflectance peak into account and relate the ratio of the elastic reflectance components at 667 and 678 nm to that at 488 and 547 nm. In that way, the new algorithms will improve their performance in the quantification of chlorophyll in coastal waters compared to the standard FLH algorithms.

The variability in fluorescence quantum yield caused by taxonomic differences, phytoplankton physiology and light exposure history (Kiefer (1973); Letelier (1996)) is resulting in an additional complexity of the relationship between chlorophyll-a and FLH. Nonetheless, Hu et al. (2005) established a robust relationship between MODIS FLH and in-situ chlorophyll-a in the west Florida Shelf waters, that yielded superior estimates of chlorophyll-a compared with standard SeaWiFS or MODIS band-ratio chlorophyll-a. They were able to use FLH to differentiate between dark features on enhanced RGB images produced by high chlorophyll-a and those produced by high CDOM.

Recently, methods were developed to detect chlorophyll fluorescence in water from hyperspectral satellite measurements. Wolanin et al. (2015) uses the filling-in of Fraunhofer lines in order to detect fluorescence from SCIAMACHY measurements. Erickson et al. (2019) on the contrary, uses the shape of the fluorescence peak for the retrieval of a fluorescence efficiency profile from TROPOMI. However, existing hyperspectral satellite data generally suffers from poor spatial resolution and signal-to-noise ratio.

The Earth observation satellites Sentinel-3A and Sentinel 3B both carrying the Ocean and Land Colour Instrument (OLCI) on board were launched in February 2016 and April 2018, respectively. The primary mission of OLCI is the observation of the spectral distribution of up-welling radiance just above the sea surface (the water-leaving radiance) which is then used to estimate geophysical parameters through the application of bio-optical algorithms. OLCI spectral bands are optimised to measure ocean colour over the open ocean and coastal zones. A band at 673 nm has been added to better capture the chlorophyll fluorescence peak. Yet, no algorithm takes full advantage of the improved spectral capacities of OLCI for the detection of fluorescence.

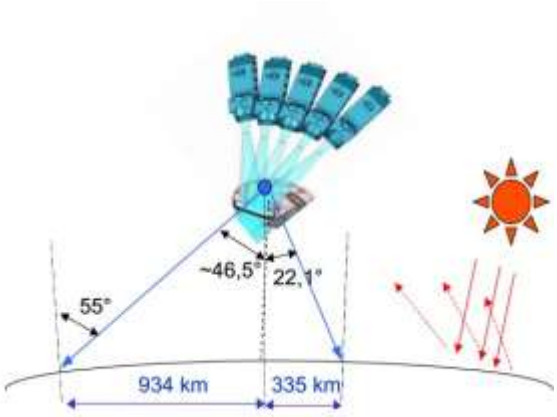


Figure 1: OLCI features a tilted field of view to avoid sun-glint

# 2 Sentinel-3 OLCI benefits for fluorescence retrieval

The measurements of the satellite sensor OLCI are described in the following with respect to the enhanced spectral resolution compared to its predecessor MERIS. The key mission objective for the Sentinel-3 OLCI instrument is the continuity of the ENVISAT MERIS instrument capability. The primary mission of OLCI is the observation of the spectral distribution of up-welling radiance just above the sea surface (the water-leaving radiance) that is then used to estimate a number of geophysical parameters through the application of specific bio-optical algorithms. The Sentinel-3 OLCI instrument is based on the opto-mechanical and imaging design of ENVISAT MERIS (see Table 1). The instrument is a quasi-autonomous, self contained, visible push-broom imaging spectrometer and incorporates the following significant improvements when compared to MERIS:

- An increase in the number of spectral bands (from 15 to 21),
- Improved SNR and a 14-bit analogue to digital converter,
- Mitigation of sun-glint contamination by tilting cameras in westerly direction by 12.6°,
- Complete coverage over both land and ocean at 300 m Full-Resolution (FR).

The cameras are arranged to slightly overlap with each other to cover a wide 68.5° across-track field of view as shown in Figure 1.

OLCI bands are optimised to measure ocean colour over the open ocean and coastal zones. A channel at 673 nm has been added for improved chlorophyll fluorescence measurement (Fig. 2). In principle, the OLCI programmable acquisition design allows spectral bands to be redefined in both location and width during commissioning of the instrument after which time they will be fixed for the mission duration. The five bands which are suitable for OC-Fluo are bands Oa8-12 (665, 673.75, 681.25, 708.75 and 753.75 nm). In order to reproduce the low signal associated with fluorescence, these bands must have a high SNR. The bands should be relatively narrow to bypass absorption features in the atmosphere and they should be stable in terms of both bandwidth and position because of the spectral proximity of these absorption features. The OLCI instrument meets these requirements.

## 2.1 Assessment of Instrument Benefits and Capabilities wrt the Product

For the design of MERIS, the ancestor of OLCI, the 681 nm band was positioned in order to include the peak of fluorescence, while avoiding the strong oxygen absorption feature at 687 nm and longer wavelengths Gower and King (2007b). OLCI additionally provides band Oa9 at 673 nm within the spectral range around the fluorescence emission peak. The spectral bands of OLCI

| Band # | λ center | Width | Lmin | Lref | Lsat | SNR@Lref |
|---|---|---|---|---|---|---|
| | nm | nm | W/(m².sr.µm) | W/(m².sr.µm) | W/(m².sr.µm) | |
| Oa1 | 400 | 15 | 21.60 | 62.95 | 413.5 | 2188 |
| Oa2 | 412.5 | 10 | 25.93 | 74.14 | 501.3 | 2061 |
| Oa3 | 442.5 | 10 | 23.96 | 65.61 | 466.1 | 1811 |
| Oa4 | 490 | 10 | 19.78 | 51.21 | 483.3 | 1541 |
| Oa5 | 510 | 10 | 17.45 | 44.39 | 449.6 | 1488 |
| Oa6 | 560 | 10 | 12.73 | 31.49 | 524.5 | 1280 |
| Oa7 | 620 | 10 | 8.86 | 21.14 | 397.9 | 997 |
| Oa8 | 665 | 10 | 7.12 | 16.38 | 364.9 | 883 |
| Oa9 | 673.75 | 7.5 | 6.87 | 15.70 | 443.1 | 707 |
| Oa10 | 681.25 | 7.5 | 6.65 | 15.11 | 350.3 | 745 |
| Oa11 | 708.75 | 10 | 5.66 | 12.73 | 332.4 | 785 |
| Oa12 | 753.75 | 7.5 | 4.70 | 10.33 | 377.7 | 605 |
| Oa13 | 761.25 | 2.5 | 2.53 | 6.09 | 369.5 | 232 |
| Oa14 | 764.375 | 3.75 | 3.00 | 7.13 | 373.4 | 305 |
| Oa15 | 767.5 | 2.5 | 3.27 | 7.58 | 250.0 | 330 |
| Oa16 | 778.75 | 15 | 4.22 | 9.18 | 277.5 | 812 |
| Oa17 | 865 | 20 | 2.88 | 6.17 | 229.5 | 666 |
| Oa18 | 885 | 10 | 2.80 | 6.00 | 281.0 | 395 |
| Oa19 | 900 | 10 | 2.05 | 4.73 | 237.6 | 308 |
| Oa20 | 940 | 20 | 0.94 | 2.39 | 171.7 | 203 |
| Oa21 | 1020 | 40 | 1.81 | 3.86 | 163.7 | 152 |

Figure 2: The spectral bands of OLCI and MERIS

around the fluorescence emission central wavelength are shown in Figure 3 with overlaying remote sensing reflectance spectra. The four bands depicted are band Oa8 – 11. The simulations are performed using the RTM MOMO (Hollstein and Fischer (2012)) and implementing a bio-optical model where chlorophyll concentration is coupled to CDOM absorption and particle scattering. For increasing chlorophyll concentration, band Oa9 becomes increasingly necessary in order to be able to capture the whole shape of the spectrum, including the local minimum between band Oa8 and Oa9, which is caused by the chlorophyll absorption peak centered at 673 nm.

As discussed before, the standard FLH approaches are affected by water constituent concentrations, because the peak around 682 nm is not only caused by fluorescence, but it is also an effect of being in a spectral minimum of combined water, CDOM and chlorophyll absorption, while the increase in this band is, despite of fluorescence, caused by scattering of water molecules and suspended matter. The three bands are not providing enough information for the separation of those different optically active substances. The inclusion of the OLCI Oa9 band at 673 nm and implementation of a more complex algorithm, was planned to allow a better separation of the fluorescence signal from scattering and absorption of chlorophyll. However, it was shown, that the new band does only provide additional useful information to model fluorescence more accurately for extremely high chlorophyll concentrations (see section 4.6.2). However, this algorithm is aimed to be able to capture the fluorescence signal more accurately and over a wider concentration range compared to the MERIS and MODIS FLH algorithms.

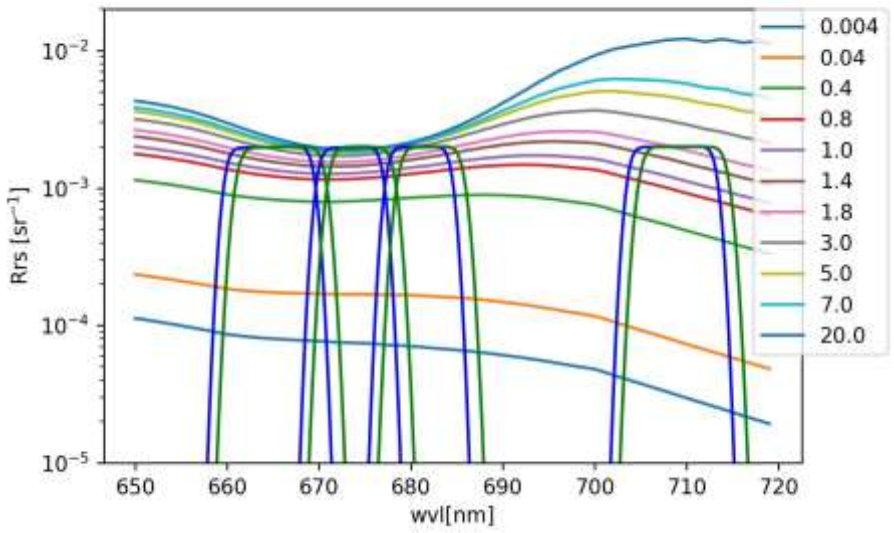


Figure 3: The spectral bands of OLCI (blue and green) with overlaying remote sensing reflectance spectra, simulated for different concentrations of chlorophyll. OLCI bands are plotted in blue and green to show the extent of band central wavelength shifts across the camera field of view due to the smile effect.

# 3 Algorithm Description

In-water chlorophyll Fluorescence is unique in its spectral shape and restriction to a distinct and narrow wavelength range. Other inherent optical properties (IOP's) in the water have comparably flat spectral features. Also the atmospheric influence is mostly spectrally flat (a water vapour correction for band 10 at 709 nm is also delivered by the institute of space sciences). Solely chlorophyll absorption induces another narrow spectral feature in the vicinity of the fluorescence peak. The presented algorithm utilizes the fact that chlorophyll causes the only spectrally high varying features in the 650-750 nm spectral range and allows us to be independent of absolute values and therefor of atmospheric correction. We apply a simple curve fit to the measurements of reflected sunlight. Two Gaussian functions of defined width and spectral position capture chlorophyll absorption and fluorescence, while all other optical influences, are covered by an offset and a slope.

## 3.1 Processing Outline

Due to the arguments from the last section, both, Level-1B and Level-2 data can be processed by the OC-Fluo algorithm. In either cases the input is the radiance or reflectance in bands Oa8-12 masked by Level-2 flags. For Level-1 data it is necessary to apply a cloud mask and additional flags, that are taken from Level-2. The following Water Quality Science Flags (WQSF) are applied:

- INVALID
- LAND
- CLOUD

The algorithm does not flag negative values of $\rho_w$, since the algorithm can give reasonable

results also with negative $\rho_w$, when the spectral shape of the data is preserved. Then the five component measurement vector of each pixel is multiplied by the Jacobian, resulting in four fitting parameters and a covariance matrix from which the uncertainties are calculated.

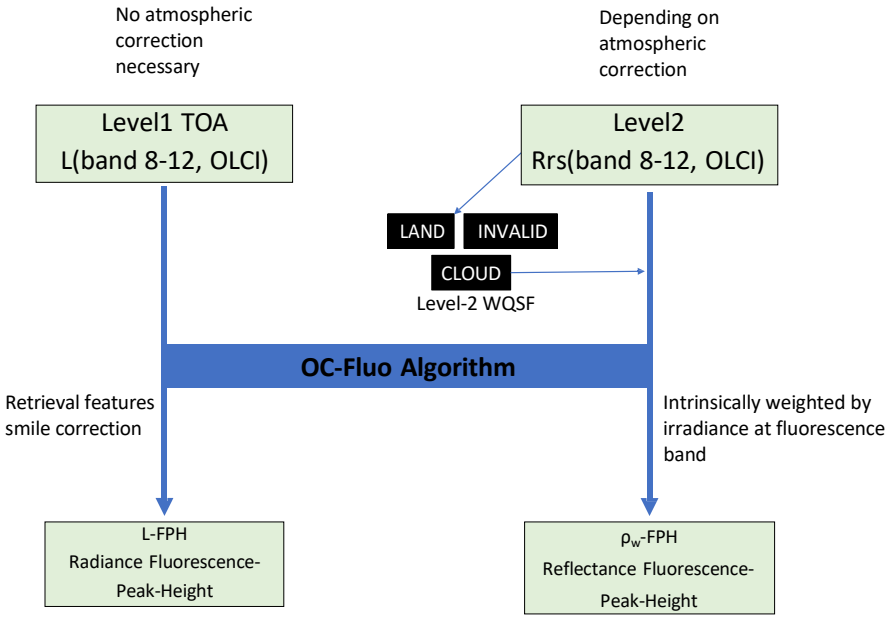


Figure 4: Processing by OC-Fluo for different input and output Levels

## 3.2 Algorithm Input

The OC-Fluo algorithm is specifically developed for OLCI measurements, but the methodology can be adapted to different sensors that measure in sufficient spectral resolution in the spectral region around the fluorescence peak. At least five bands covering the chlorophyll absorption dip and the fluorescence peak between 650 and 750 nm are required. We prepare, test and
validate the algorithm for L-FPH and $\rho_w$-FPH. The fluorescence algorithm uses two OLCI standard products:

- Level-1B product

  The Level-1 product provides contain calibrated, ortho-geolocated and spatially re-sampled Top Of Atmosphere (TOA) radiances for the 21 OLCI spectral bands, plus annotation data associated to OLCI pixels. From the annotation data we use instrument features and settings for further processing such as detector index or OLCI channels, central wavelength and bandwidths and the solar flux.

- Level-2 water products

  The Level-2 water product provides directional water reflectances, bio-optical and atmospheric parameters (see also sec. 3.1).

## 3.3 Theoretical Description

### 3.3.1 Physical Description

The physical basis of the presented algorithm is the law of Lambert-Beer, which describes extinction of electromagnetic radiation by matter.

$$I = I_0 e^{-\sigma_i(\lambda) n_i L} \tag{3}$$

Here $I_0$ is incoming and I is outgoing intensity. $\sigma_i$ is the attenuation cross section of the attenuating species i in the material sample; $n_i$ is the number density of the attenuating species i in the material sample; L is the path length of the beam of light through the material sample. The equation can be written as

$$\sigma(\lambda) nL = \log(I_0/I) \tag{4}$$

In atmospheric remote sensing it is quite common to use an approach called DOAS (Differential optical absorption spectroscopy), where the individual absorption cross sections of trace gases are fitted to the logarithm of $I/I_0$. The separation of different species is possible because each gas has it's unique spectral finger print. Chlorophyll fluorescence also has a unique spectral shape. The inherent optical properties (IOPs) of the main water constituents as they are implemented in the Radiative Transfer Model (RTM) MOMO (Fischer et al. (2010), see also chapter Validation) are shown in figure 5. The IOPs were chosen so that the spectral variability expected in nature can be reproduced by the model. There is chlorophyll fluorescence, which is an elastic process and can be described as a Gaussian curved source in radiative transfer. Three spec- trally different absorbers are shown in figure 5. Chlorophyll is described through a measured absorption spectrum, detritus and CDOM are both represented by an exponential decay with slightly different slopes. Scattering on particles follows spectrally an inverse function. These shapes are in the retrieval reproduced by simple geometrical functions.

For the Fluorescence retrieval we are not operating in logarithmic space, which is possible because the light path of the photons throughout the complete wavelength range of interest is similar. We are using either radiance ( I) or reflectance ( $I/I_0$), which is justified by the assumption that the spectral features, which are extracted by the retrieval, are induced only by the water body.

### 3.3.2 Mathematical Description

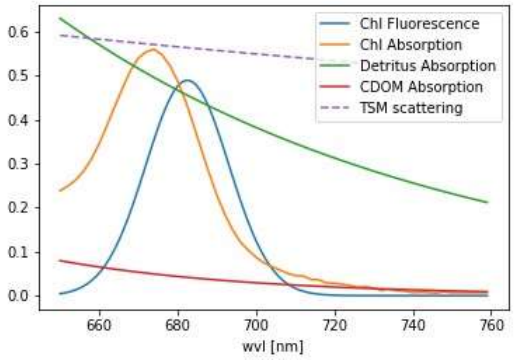


Figure 5: Optical properties of water constituents.

- $\vec{x}$ expresses the state vector, which includes the parameters to be retrieved.
- $\vec{y}$ expresses the measurement vector, which includes the measurements.
- $F_{mod}$ is the forward model, which describes $\vec{y}$ as a function of $\vec{x}$

$$F_{mod}(\lambda, \vec{x}) = \vec{y}(\lambda) \tag{5}$$

The measured radiance or reflectance (the equation only expresses radiance for clarity) is described as a function of 4 unknown (state) parameters:

- O = offset, accounting for atmospheric and oceanic scattering processes
- S = slope gradient, accounting for atmospheric and oceanic scattering processes and absorption
- APD = amplitude of Gaussian function at $\lambda_A$ (absorption minimum of chlorophyll)
- FPH = amplitude of Gaussian function at $\lambda_F$ (chlorophyll fluorescence peak)

and 4 fixed model parameters:

- $\lambda_A$ = center wavelength of the Gaussian absorption maximum of chlorophyll in the red = 673.5 nm
- $\lambda_F$ = center wavelength of the Gaussian fluorescence maximum of chlorophyll = 682.5 nm
- $w_F = 2c_F^2 = 416$ nm, with $c_F$ being the standard deviation of the Gaussian fluorescence of chlorophyll
- $w_A = 2c_A^2 = 250$ nm, with $c_A$ being the standard deviation of the Gaussian absorption of chlorophyll

The forward model is composed of two Gaussian functions, a slope and an offset (see also Figure 6):

$$L_{TOA}(\lambda) = O + S \cdot \lambda + APD \cdot \exp((\lambda - \lambda_A)^2/w_A) + FPH \cdot \exp((\lambda - \lambda_F)^2/w_F) \tag{6}$$

The unknown parameter FPH in eq. 6 defines the fluorescence product. Figure 6 shows the

components of the curve retrieved by the fit.

(7)

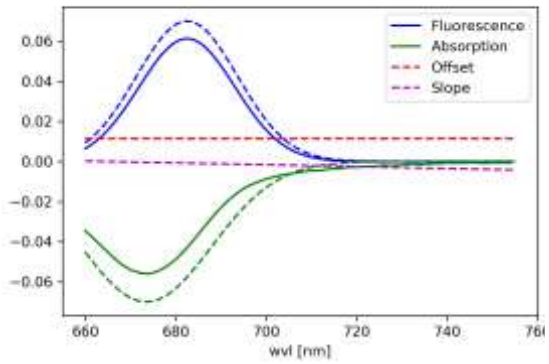


Figure 6: Components of the curve, that is fitted to the radiance spectrum.

## 3.4 Technical Description

Technically the retrieval is based on an optimal estimation approach. We define a measurement and a state vector. The measurement vector y is given by OLCI data band 8-12 and the state x is defined by the factor for fluorescence (FPH), absorption (APD), a slope (S) and an offset (O).

$$measurement = \vec{y} = \begin{pmatrix} Oa08\_reflectance \\ Oa09\_reflectance \\ Oa10\_reflectance \\ Oa11\_reflectance \\ Oa12\_reflectance \end{pmatrix}$$

$$state = \vec{x} = \begin{pmatrix} O \\ S \\ APD \\ FPH \end{pmatrix}$$

Equations (7) and (8).

The Jacobian is the derivative matrix of the measurement to the state. Each line of this matrix is the derivative of the forward function to the corresponding state parameter.

(9)

$$\mathbf{K} = \begin{pmatrix} \partial y_1/\partial x_1 & \partial y_2/\partial x_1 & \partial y_3/\partial x_1 & \partial y_4/\partial x_1 & \partial y_5/\partial x_1 \\ \partial y_1/\partial x_2 & \partial y_2/\partial x_2 & \partial y_3/\partial x_2 & \partial y_4/\partial x_2 & \partial y_5/\partial x_2 \\ \partial y_1/\partial x_3 & \partial y_2/\partial x_3 & \partial y_3/\partial x_1 & \partial y_4/\partial x_3 & \partial y_5/\partial x_3 \\ \partial y_1/\partial x_4 & \partial y_2/\partial x_4 & \partial y_3/\partial x_4 & \partial y_4/\partial x_4 & \partial y_5/\partial x_4 \end{pmatrix}$$

and therefore:

$$\mathbf{y} = \mathbf{K}\bar{\mathbf{x}} \qquad (10)$$

Inserting Eq. 6 gives:

$$\mathbf{K} = \begin{pmatrix} 1 & 1 & 1 & 1 & 1 \\ (\lambda_8 - \lambda_S)/1000. & (\lambda_9 - \lambda_S)/1000. & (\lambda_{10} - \lambda_S)/1000. & (\lambda_{11} - \lambda_S)/1000. & (\lambda_{12} - \lambda_S)/1000. \\ exp((\lambda_8 - \lambda_A)^2/w_A & exp((\lambda_9 - \lambda_A)^2/w_A & exp((\lambda_{10} - \lambda_A)^2/w_A & exp((\lambda_{11} - \lambda_A)^2/w_A & exp((\lambda_{12} - \lambda_A)^2/w_A \\ exp((\lambda_8 - \lambda_F)^2/w_F & exp((\lambda_9 - \lambda_F)^2/w_F & exp((\lambda_{10} - \lambda_F)^2/w_F & exp((\lambda_{11} - \lambda_F)^2/w_F & exp((\lambda_{12} - \lambda_F)^2/w_F \end{pmatrix} \qquad (11)$$

For the application of this algorithm to OLCI measurements $\lambda_8 - \lambda_{12}$ are given by the nominal wavelength of band Oa8-12 (665.0 nm, 673.75 nm, 681.25 nm, 708.75 nm, 753.75 nm). In order to keep computation time low, we assume this values to be constant (for the inherent smile correction see Sec. 3.6). Inserting the values for $\lambda_F$, $\lambda_A$, $w_F$ and $w_A$ gives:

$$\mathbf{K} = \begin{pmatrix} 1 & 1 & 1 & 1 & 1 \\ 0 & 8.8 \cdot 10^{-3} & 1.63 \cdot 10^{-2} & 4.38 \cdot 10^{-2} & 8.88 \cdot 10^{-2} \\ -8.4 \cdot 10^{-1} & -1 & -8.7 \cdot 10^{-1} & -5.04 \cdot 10^{-2} & -1.89 \cdot 10^{-7} \\ 2.94 \cdot 10^{-1} & 7.36 \cdot 10^{-1} & 9.94 \cdot 10^{-1} & 6.35 \cdot 10^{-2} & 1.52 \cdot 10^{-9} \end{pmatrix} \qquad (12)$$

$\mathbf{K}$ is a rectangle matrix with full row rank and thus features a right inverse $\mathbf{K}^{-1}_{right} = \mathbf{K}^T(\mathbf{K}\mathbf{K}^T)^{-1} = \mathbf{K}^{-1}$, so that the state vector $\bar{\mathbf{x}}$ can be derived from:

$$\bar{\mathbf{x}} = \mathbf{K}^{-1}\bar{\mathbf{y}} \qquad (13)$$

In principle, the number of channels that are included in the measurement vector is flexible and can be adapted according to the sensor. The number of measurements (bands) must be equal or larger than the number of state parameters to be retrieved (possible additional parameters are $\lambda_A$, $\lambda_F$, $w_F$, $w_A$, see equation 6) in order to get a K-matrix that is invertible.

## 3.5 Spectral solar Irradiance ($F_0$) weighting for the L-FPH product

The spectral distribution of the solar irradiance is known and the seasonally corrected In-band solar irradiance ($F_0(\lambda)$) is delivered with Level-1 OLCI data. In order to compensate for spectral structures introduced by $F_0$ that could interfere with optical properties of chlorophyll, the pre-processing for the retrieval of L-FPH includes a rectification with a normalised $F_0(\lambda)$. In practice $L_{TOA}$ are divided by $F_0(\lambda)$ and multiplied by $F_0$ in band 682nm.

1. $L_T$OA are divided by "In-band solar irradiance, seasonally corrected" in instrumentdata.nc.
2. $L_T$OA are multiplied by mean solar irradiance in band 682 nm.

$$L^*_{TOA}(\lambda) = L_{TOA}(\lambda)/F_0(\lambda) * F_0(682nm) \qquad (14)$$

## 3.6 The smile correction for the L-FPH product

OLCI consists of five optical modules, of which each exhibits a variation of the relative spectral

response of the bands in the field of view. This variation is further different for each module ? The camera to camera variations in the central spectral wavelength as well as additional small variations in each detector array are visible as stripes across swath. Those variations, up to 1.5 nm are hardly visible when looking at the whole spectral range, but they can be important when spectrally narrow features are measured with spectrally narrow channels. Accordingly the stripes can be visible in the results from algorithms assuming measurements at nominal wavelength as it is the case for the presented algorithm. Level-1 data is delivered including the central wavelength for each pixel. Operationally Level-2 data is smile corrected assuming a linear relationship between Rayleigh corrected reflectances in neighbouring bands (Bourg et al., 2010). With this assumption the water reflectances are corrected to the values as if they were measured at nominal wavelengths.

However Level-1b data is delivered without smile correction. Therefore we developed and implemented an internal smile correction for Level-1b data. The internal OC-Fluo smile correction is based on the relationship between neighbouring bands defined by Eq. 6, therefore it begins technically with the application of the retrieval (equation 13) on Level-1b data ($\underline{y}_{sh}$) measured at $\lambda_{sh}$.

$$\underline{x}_{sh} = K^{-1}\underline{y}_{sh} \tag{15}$$

With the resulting state $\bar{\underline{x}}_{sh}$. Assuming that the forward modelled spectrum based on $\bar{\underline{x}}_{sh}$ represents the slope from measured to nominal wavelength, the shift in radiance units can be calculated from the shift in wavelength through $F_{mod}$:

$$\Delta L_{TOA}(\lambda) = F_{mod}(\lambda, \underline{x}_{sh}) - F_{mod}(\lambda_{sh}, \underline{x}_{sh}) \tag{16}$$

This $\Delta L_{TOA}$ is then added to the measured $L^{*}_{TOA}$.

$$L_{TOA,corr}(\lambda) = L_{TOA}(\lambda) + \Delta L_{TOA}(\lambda) \tag{17}$$

$L_{TOA,corr}(\lambda)$ is now input to the retrieval. As an example for the effectiveness of this smile correction, Fig. 7 shows a detail of the Barents Sea scene (Fig. ??), which is also used for evaluation (see Sec. 4.2) with L-FPH, which was smile corrected by our retrieval and $\rho_w$-FPH, where the boundary of two cameras is still visible despite of the Level-2 smile correction.

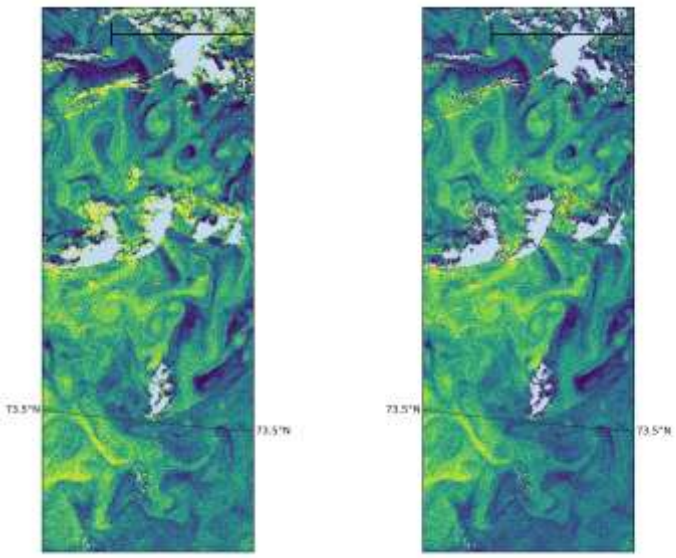

Figure 7: Comparison of the internal smile correction on Level-1b data and the standard smile correction of OLCI Level-2 data, through the comparison of the two different products in a detail of the Barents Sea scene (Fig. ??) with L-FPH (left panel) and $\rho_w$-FPH (right panel), where the boundary of two cameras is visible in the $\rho_w$-FPH but not in the L-FPH.

## 3.7 Algorithm Output

The OC-Fluo python script returns a netcdf file in a structure that is readable by SNAP. It includes pixel-wise values for L-FPH, $\rho_w$-FPH, Chl from L-FPH, Chl from $\rho_w$-FPH, L-APD, $\rho_w$-APD.

For product description see section 1.1 As depicted in Fig. 4, Level-1 TOA radiances, as input parameter, result in L-FPH. Level-2 $\rho_w$, as input parameter, result in $\rho_w$-FPH. Both quantities are validated in section 4.2.

### 3.7.1 Sensor Effects

- Instrumental noise
  How instrumental noise propagates into retrieval uncertainty is described in section 3.7.2.
- Smile effect
  Due to the optical design of OLCI, which is a medium resolution imaging spectrometer, all spectral bands show a slightly varying central wavelength over the field of view (the smile effect). Since each camera possesses individual wavelength characteristics, prominent wavelength jumps of up to one nanometer between cameras occur. OLCI Level-2 water reflectances are smile corrected by a linear approach in the L2 processing. For the OC-Fluo algorithm, an independent smile correction has been designed (see Section 3.6). According to Kritten and Preusker (2017) the OLCIs smile effect may cause in extreme cases of high chlorophyll ($> 100$ µg/l) an error of up to 5%, but this can be reduced by applying the standard smile correction to band Oa10.

### 3.7.2 Retrieval Errors

Following a Gaussian error retrieval, we calculate the error covariance as follows

$$S = (K^T S_e^{-1} K)^{-1} \quad (18)$$

with the diagonal elements of $S_e$ being the absolute noise of the measurement. Assuming a SNR of 63 for full resolution images, this results in around 10% uncertainty for both L-FPH and $\rho_w$-FPH. Since we are using a linear forward model, K is a constant and therefore S is a constant as well.

# 4 Validation

## 4.1 Challenges for the validation of satellite based chlorophyll fluorescence

While validation is always a challenge, it is especially difficult in the case of measuring fluorescence from space. Remote sensing products are customarily validated against a ground truth. But Fluorescence is not an IOP, because it is not a property of the water body alone, but also a property of current and historical illumination. We do not have an independent ground truth for fluorescence, since this light emission is a response to photoinhibition, which is easily influenced by the in-situ measurement process. In-situ fluorescence measurements are governed by active light pulses and therefor not comparable to sun-induced fluorescence. The common approach to validate fluorescence from satellite based measurements is the comparison to chlorophyll concentration. Here, the strong correlation of chlorophyll fluorescence to chlorophyll concentration is employed, although the conversion of one measure to the other can vary by a factor of eight and there are a variety of factors influencing this.

## 4.2 Validation approach

The validation, as it could be performed in the scope of this study, is an evaluation of the algorithm and its products on different levels using multiple sources. Neither of the validations compares two identical measures.

1. Correlation with in-situ HPLC chlorophyll measurements
2. Correlation with standard OLCI chlorophyll products OC4me and NN
3. Inter-comparison with MODIs nFLH product (the only validation with another fluorescence measure)
4. Correlation with chlorophyll from RTM

As it is common practice for the validation of remote sensing products, the main validation of the Fluorescence products, L-FPH and $\rho_w$-FPH is performed through the comparison to in-situ measurements, but in this case, of chlorophyll concentration. The comparison to chlorophyll is state-of-the-art for the validation of fluorescence algorithms (see section 1.3). The fluorescence is expected in first order to be correlated to chlorophyll concentration. For the in-situ matchup comparison this chlorophyll concentration is the result of HPLC measurements. Additional to the default flags (see sec. 1.1), flags as recommended in EUMETSAT (2019) are applied for the validation against in-situ data (see section 4.3.1). Additionally, L-FPH and $\rho_w$-FPH are correlated to chlorophyll from the two standard operational Level-2 chlorophyll processors for OLCI, OC4me and Neural Network. Only in the comparison of L-FPH, $\rho_w$-FPH and MODIS nFLH two

fluorescence measures are compared to each other. Finally $\rho_w$-FPH is compared to the input chlorophyll from RTM simulations.

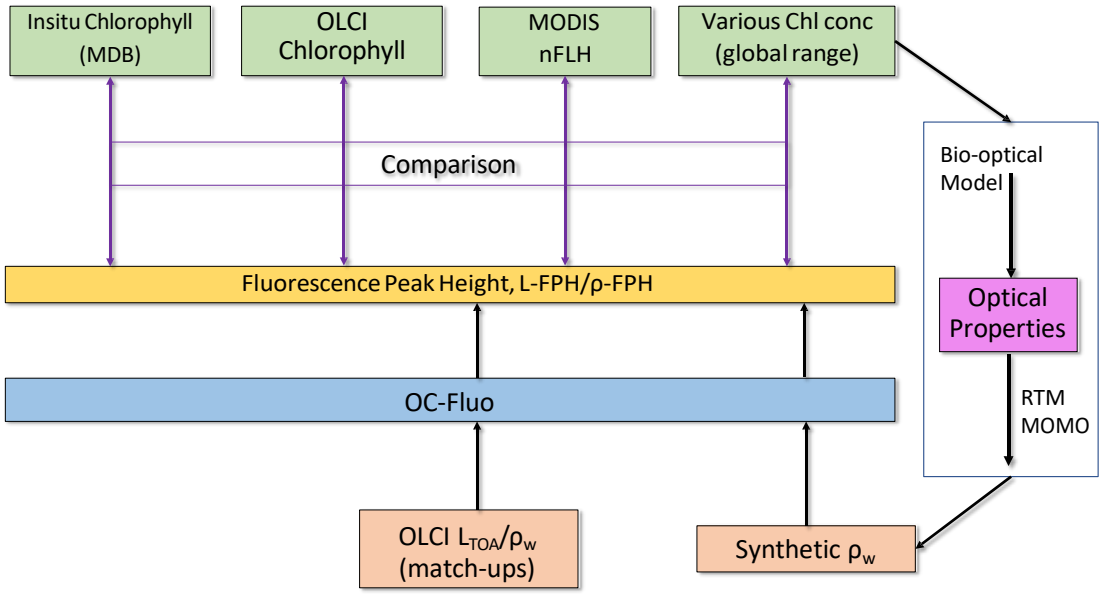


Figure 8: Validation approach for the OC-Fluo algorithm.

## 4.3 Validation against in-situ matchups

### 4.3.1 HPLC Matchup Database MDB

The main data set for the validation of the OC-Fluo algorithm is the HPLC Matchup Database (MDB) which includes HPLC data from NASA SeaBASS Werdell et al. (2003) with OLCI matchups (Eumetsat Ocean Color In-situ Database, 2019) and is available at https://ocdb.eumetsat.int/. Most of the matchups are located in Santa Barbara Gulf in California (PIs David Siegel, Emmanuel Boss and Lynne Talley are gratefully acknowledged). Thus they are not representative for all kinds of waters, but they are very well distributed throughout seasons providing examples of different levels of chlorophyll-a concentration. The HPLC Matchups DataBase (HPLC MDB) is distributed by a netCDF file, providing both OLCI data (25 x 25 pixel centred over in-situ coordinates) and in-situ data. All variables are included as they are in the original OLCI Level-2 products. HPLC measurements are optically weighted to provide a unique value when multiple casts are provided within a radius of 150 m within 1 hour from the first measurement below the surface. A ±3-h window is assigned around the satellite overpass as condition for coincidence. Only in-situ measurements are included where at least one measurement in the top layer is available. For the satellite matchups, we follow the OLCI matchup protocol (EUMETSAT, 2019).

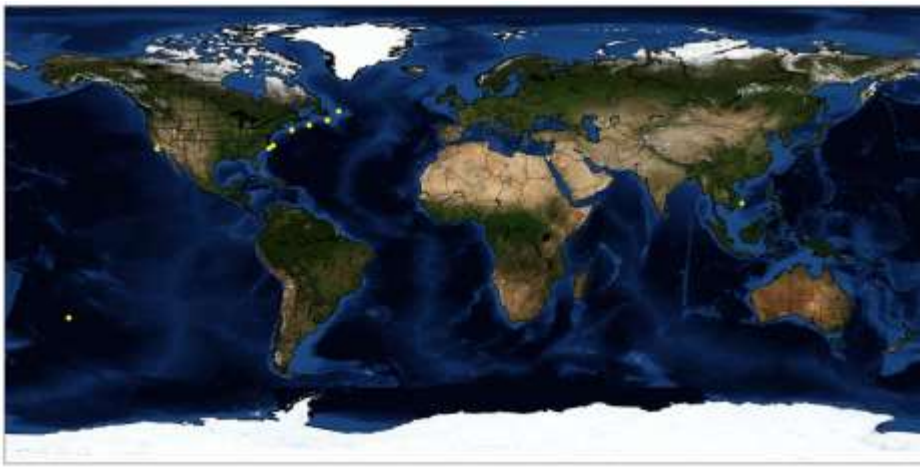

Figure 9: World map with locations of HPLC measurements extracted from SeaBASS database.

A box of 5x5 pixels is defined, centered on the location of the in-situ measurement. This box allows for the generation of simple statistics, such as the mean and standard deviation, to as- sist in the evaluation of spatial stability, or homogeneity, at the validation point. On a pixel basis we applied the suggested Level-2 WQSF flags: CLOUD, CLOUDAMBIGUOUS, CLOUDMAR- GIN, INVALID, COSMETIC, SATURATED, SUSPECT, HISOLZEN, HIGHGLINT, SNOWICE, ACFAIL, WHITE- CAPS, ANNOTABSOD, ANNOTMIXR1, ANNOTTAU06, RWNEGO2, RWNEGO3, RWNEGO4, RWNEGO5, RWNEGO6, RWNEGO7, RWNEGO8, OC4MeFAIL. Only measurements are included where the sensor zenith is $< 60°$ and sun zenith $< 70°$. Fig. 9 shows a map with the locations of the remaining 30 valid HPLC measurements extracted from the SeaBASS database. In the Santa Barbara Gulf in California 22 measurements are made in the same area and cannot be separately displayed.

Fig. 10 shows the retrieved $\rho_w$-FPH and L-FPH from OLCI matchups over in-situ Chl concentration from global measurements. The white background shows the proposed sensitivity range.

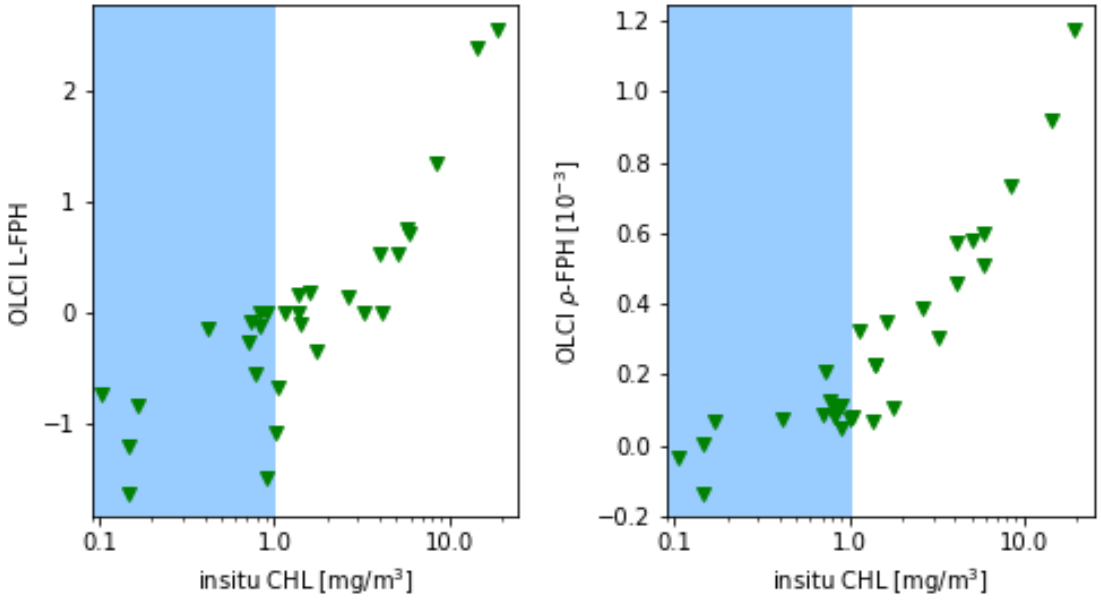


Figure 10: L-FPH from OLCI matchups over in-situ Chl concentration from HPLC measurements (left panel) and $\rho_w$-FPH from OLCI matchups over in-situ Chl concentration from HPLC measurements (right panel) from global measurements. The white background shows the proposed sensitivity range.

### 4.3.2 Transects in the Atlantic

The chlorophyll in-situ data from transects in the Atlantic Ocean are provided by Prof. Astrid Bracher, Alfred Wegener Institut, Germany. The water type here is mostly open ocean and the chlorophyll concentration is below the sensitivity range of the OC-Fluo algorithm. The data is shown here and used for validation purposes in order to show that low chlorophyll concentration does not produce unrealistic values but rather noise at lower values. Fig. 12 shows

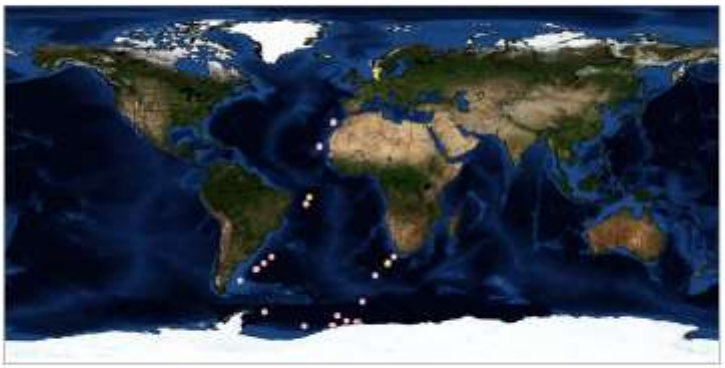

Figure 11: World map with locations of in-situ measurements from Astrid Bracher.

$\rho_w$-FPH and L-FPH over in-situ Chl concentration from transects in the Atlantic ocean. The in-situ chlorophyll concentration is mostly below the sensitivity range of the algorithm and the retrieved values are accordingly low.

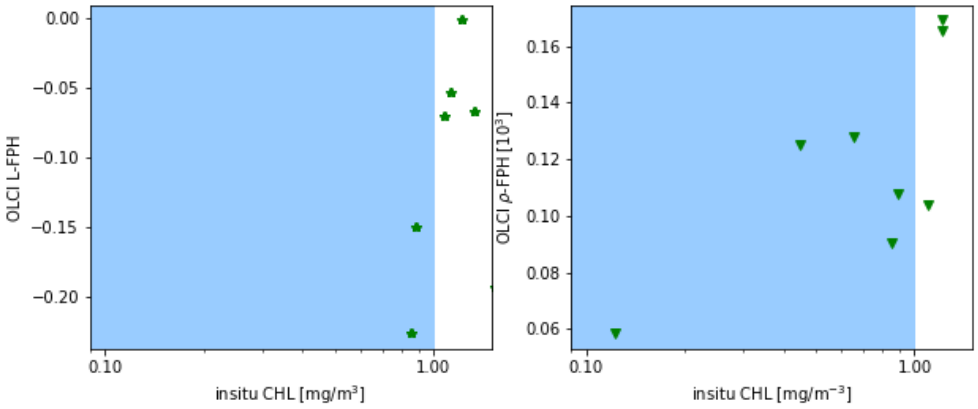


Figure 12: $\rho_w$-FPH from OLCI matchups over in-situ Chl concentration from HPLC measurements (left panel) and L-FPH from OLCI matchups over in-situ Chl concentration from HPLC measurements (left panel) from transects in the Atlantic. The white background shows the proposed sensitivity range.

Figure 13: Landsat satellite photo of Lake Peipus, from Wikipedia, 2019

### 4.3.3 In-situ Measurements in Lake Peipus

Lake Peipus is the largest transboundary lake in Europe, lying on the border between Estonia and Russia and the lake is the fifth-largest in Europe. Lake Peipus represents a remnant of a body of water which existed in this area during an Ice Age. It covers 3555 km$^2$, and has an

average depth of 7,1 m, the deepest point being 15 m. The lake has several islands and consists of 3 parts:

- Lake Peipsi/Chudskoe, the northern part of the lake, with an area of 2611 $km^2$ (73%)
- Lake Pskov, the southern part of the lake (area 708 $km^2$ or 20%)
- Lake Lämmijärv/Teploe, the sound connecting the other two parts of the lake (area 236 $km^2$ or 7%)

The lake is used for fishing and recreation, but suffered from some environmental degradation from Soviet-era agriculture. Some 30 rivers and streams discharge into Lake Peipus. The largest rivers are the Emajõgi and the Velikaya River. The lake drains into the Gulf of Finland via the Narva River. The ecological condition of the lake basin is, in general, satisfactory – water is mostly of grades I and II (clean), and is of grade III in some rivers due to the high content of phosphorus. The water condition of the rivers has improved since 2001–2007, but there is an increase in population of blue-green algae. The main problem of Lake Peipus is its eutrophication, which generally increases from north to south.

We have access to in-situ measurements in Lake Peipsi of hyperspectral in-situ reflectances and chl-a from 2016 (courtesy of Krista Alikas, Tartu Observatory, Estonia). Chl was measured spectrophotometrically with a Hitachi U-3010 spectrophotometer and chlorophyll concentration was calculated according to the method of Jeffrey and Humphrey (1975).

Unfortunately there are no valid OLCI matchups when applying the criteria from the OLCI Matchup Protocols (EUMETSAT, 2019). Therefore, we process the in-situ reflectances and compare them to in-situ chlorophyll. When evaluating the in-situ reflectances many difficulties fall away and the pure performance of the algorithm in complex waters can be tested. On the left side in Fig. 14 in-situ measured high resolution reflectance spectra are shown, from which the OC-Fluo retrieved $\rho_w$-FPH against chlorophyll from in-situ measurements is shown on the right side. For both dates $\rho_w$-FPH and chlorophyll show a very clear correlation, which is more linear in the case of the 27.7.16.

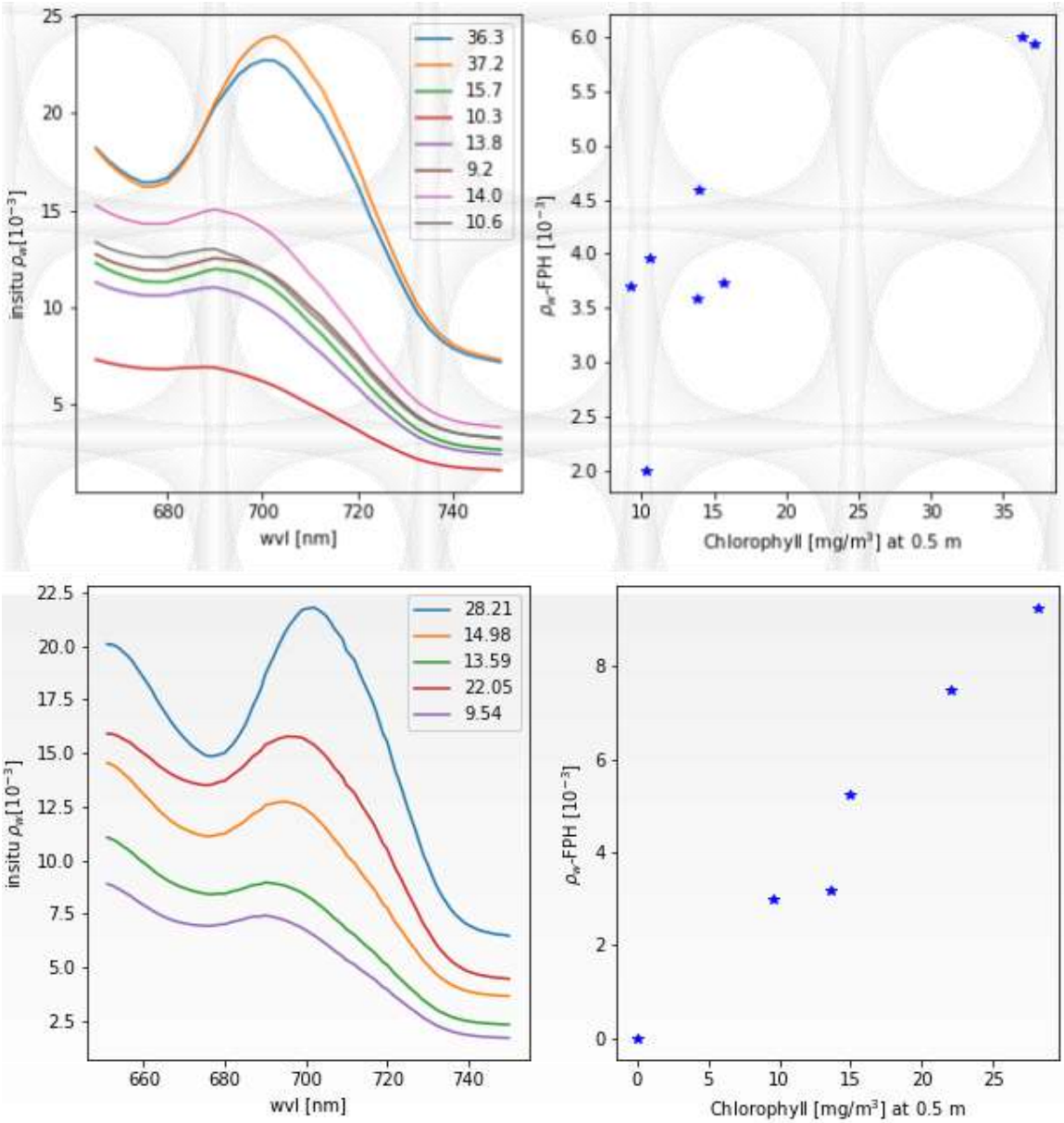


Figure 14: In-situ Rrs measured at Lake Peipus for different chlorophyll concentrations (left panel, numbers in mg/m$^3$) for the 14.6.16 (upper panels) and the 27.7.16 (lower panels) and according $\rho_w$-FPH retrieved from the in-situ Rrs over chlorophyll concentrations from in-situ measurements (right panels).

Since the assumption of homogeneity is surely not given in this case and applying OLCI matchup protocols gives no valid output, we do not include this example into the validation of the OLCI fluorescence product but show this as an example of the ability of the algorithm to give an estimate of chlorophyll concentration in inland waters. However we process the OLCI data of the respective dates, where in-situ data is available. Fig. 15 shows OLCI L-FPH on the left side in colour code with overlaying Chl concentration in mg/m$^3$ from the in-situ measurements from the 14.06.2016 in Lake Peipsi and the same for $\rho_w$-FPH on the right side. Fig. 16 shows the same for the 27.07.2016. In both cases the gradient in chlorophyll concentration from the northern to the southern part of the lake is clearly represented by the FPH. Also finer structures are visible but do not clearly correspond to the in-situ measured chlorophyll values, which is probably due to the time lag between in-situ and satellite measurement and due to the hetero-

geneity in the lake. Close to the shore, adjacency effects might also play a role.

### 4.3.4 Conclusion on the comparison to in-situ matchups

As well L-FPH as $\rho_w$-FPH from OLCI matchups show a good correlation to global in-situ measured chlorophyll, if the chlorophyll concentration is higher than $1\,mg/m^3$. L-FPH obtain negative values for low chlorophyll concentration, which is most probably a negative offset due to atmospheric spectral influence. Because of the large scatter and negative values in FPH for Chl $< 1\,mg/m^3$, we define a sensitivity range for this algorithm of Chl $> 1\,mg/m^3$. Fitting this data with a polynomial function, we deduced a relation between FPH and chlorophyll, which is also part of the processor (see ATBD sec. 5).

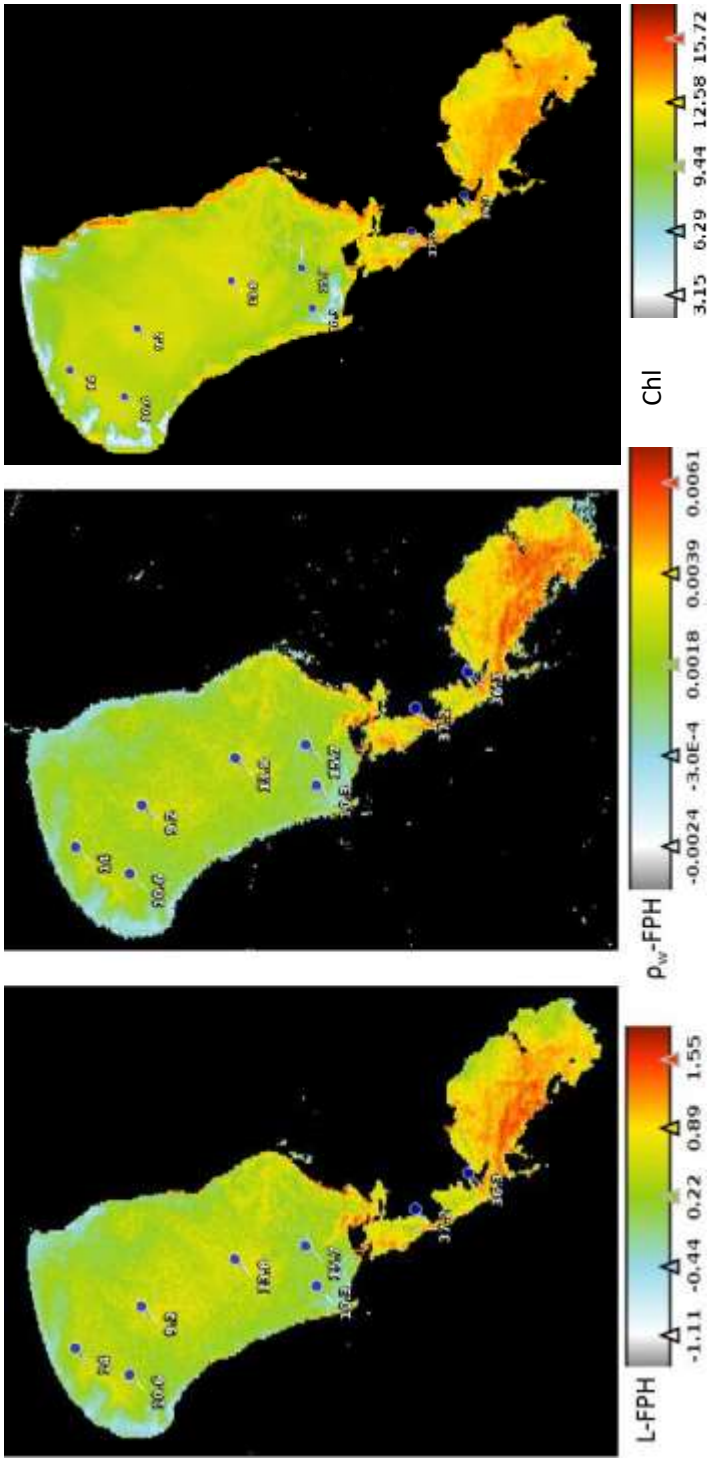


Figure 15: L-FPH (left panel) and $\rho_w$-FPH (middle panel) in Lake Peipsus retrieved by the OC-Fluo algorithm and NN chlorophyll (right panel) from OLCI data on 14.06.2016 (colour coded) and overlaying in-situ chlorophyll concentration in mg/m$^3$.

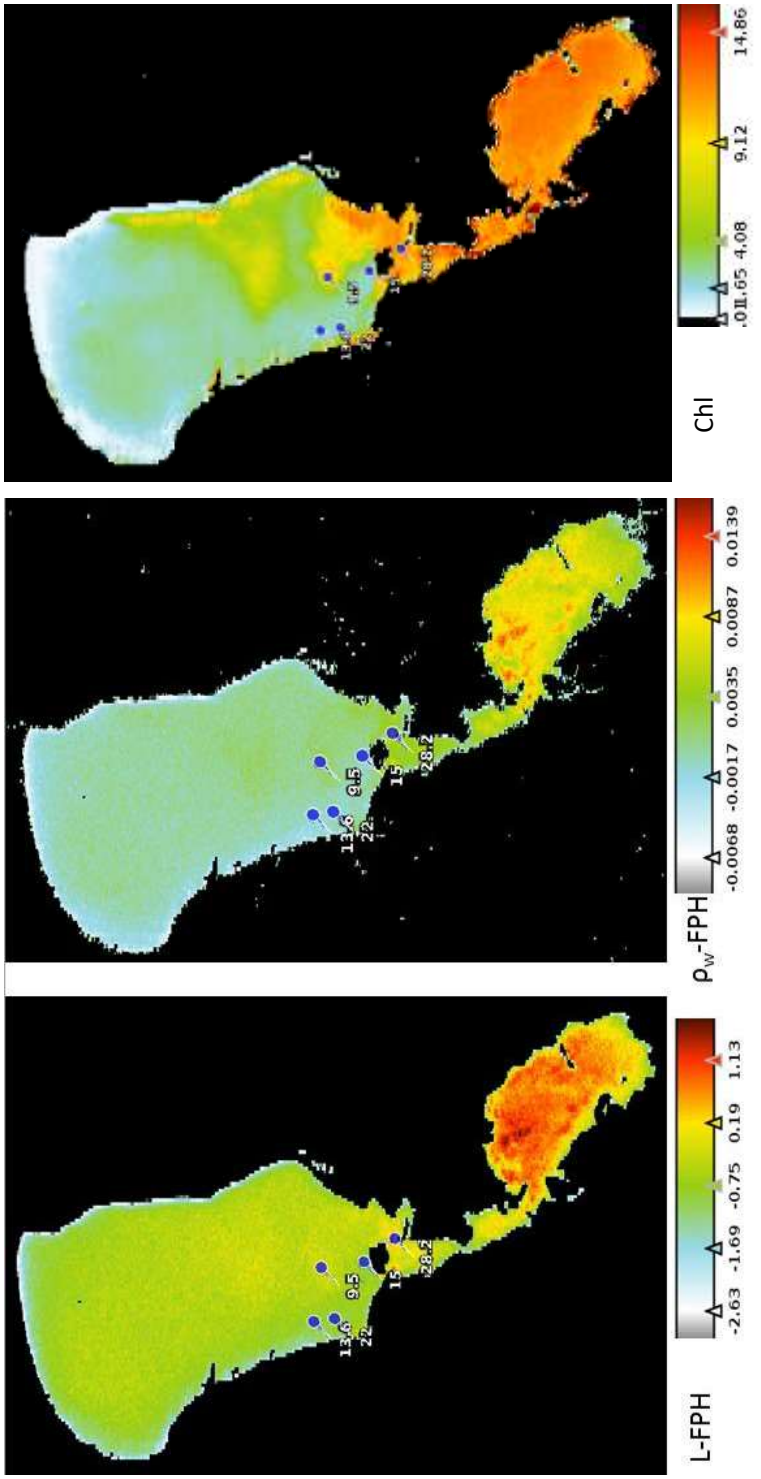


Figure 16: L-FPH (left panel) and $\rho_w$-FPH (middle panel) in Lake Peipsus retrieved by the OC-Fluo algorithm and NN chlorophyll (right panel) from OLCI data on 27.07.2016 (colour coded) and overlaying in-situ chlorophyll concentration in mg/m$^3$ from HPLC measurements at blue pins.

## 4.4 Validation against OC4Me and Neural Network (NN) Chlorophyll from OLCI

In this section we compare OC4Me and NN Chlorophyll with L-FPH and ρ-FPH by means of three example scenes with different water types. The NN Chlorophyll is estimated through an Inverse Modelling Technique based on an Inverse Radiative Transfer Model-Neural Network to estimate from normalised water-leaving reflectance at OLCI bands and among others the log10 of the absorption coefficient of algal pigment from which Chl NN is derived (Brockmann et al., 2016). OC4Me is a Maximum Band Ratio semi-analytical algorithm, developed by Morel et al. (2007). For the comparison it is important to note, that the Neural Network Chlorophyll is more relevant for complex waters, whereas OC4Me is more appropriate in open ocean waters. The three scenes used in the validations are the Rio de la Plata estuary, part of the Barents Sea and a part of the Black Sea. The scenes are displayed with only the processors default flags (see sec. 1.1) applied. In order to derive a quantitative measure, we also derive a linear correlation coefficient R. A few studies show that on a local scale a linear relationship between fluorescence and chlorophyll concentration may exist (Fischer and Kronfeld, 1990), although other studies show that this relationship is strongly nonlinear (Babin et al., 1996). As a drawback of getting a good correlation and applying a simple general relationship, we derive the linear correlation coefficient R between FPH and the logarithm of Chl. Please note, that this coefficient is not necessarily a measure of the quality of the retrieval. For this pixel-wise correlation the OLCI matchup protocol (EUMETSAT, 2019) is applied.

### 4.4.1 Rio de la Plata

The South Atlantic Ocean near the Rio de la Plata Estuary is a highly dynamic and complex region that encompasses both Case 1 and Case 2 water types. This scene is characterized by extremely high, but also very low values of chlorophyll. Chlorophyll as a product from the OC4Me and NN processor on the 26th of November, 2017 is shown in Fig. 17. The concentration reaches from 0.1 $mgm^{-3}$ in the open ocean to 25 $mgm^{-3}$ in the estuary. L-FPH and $\rho_w$-FPH are shown in Fig. 18, also with highest values in the estuary. The patterns of L-FPH and $\rho_w$-FPH look similar to NN Chlorophyll, with an indication of a better resolution of high values for the FPH products. The correlation of L-FPH and $\rho_w$-FPH to Chlorophyll from OC4Me and NN is shown in Fig. 19. There is a clear correlation between FPH and NN Chlorophyll. Both, the correlation coefficient R between L-FPH and Chlorophyll from NN and Chlorophyll from OC4Me is 0.86. The correlation coefficient R between $\rho_w$-FPH and Chlorophyll from NN and Chlorophyll from OC4Me is 0.87.

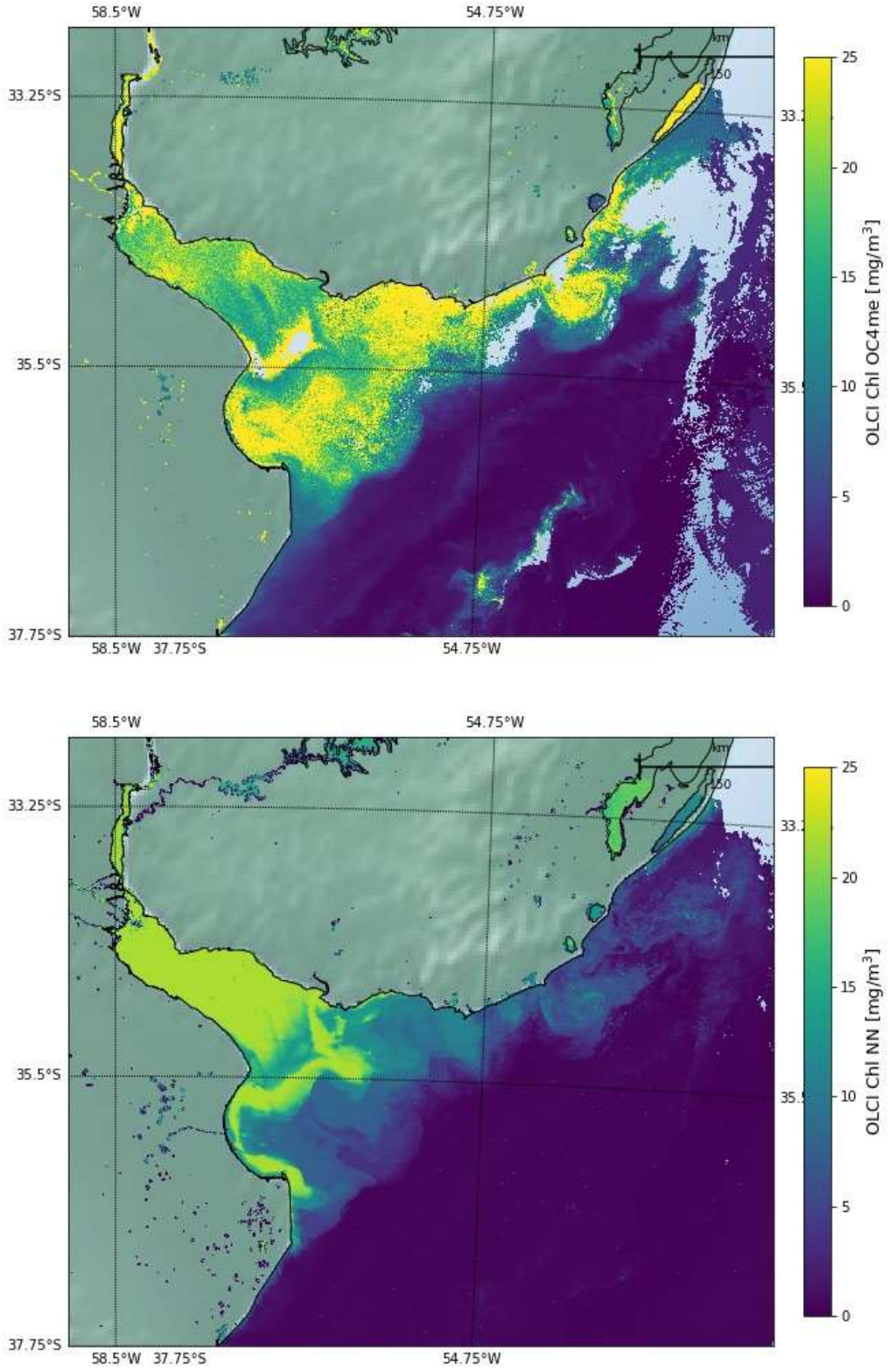


Figure 17: Chlorophyll Rio de la Plata from OC4Me (upper panel) and Neural Net processor (lower panel)

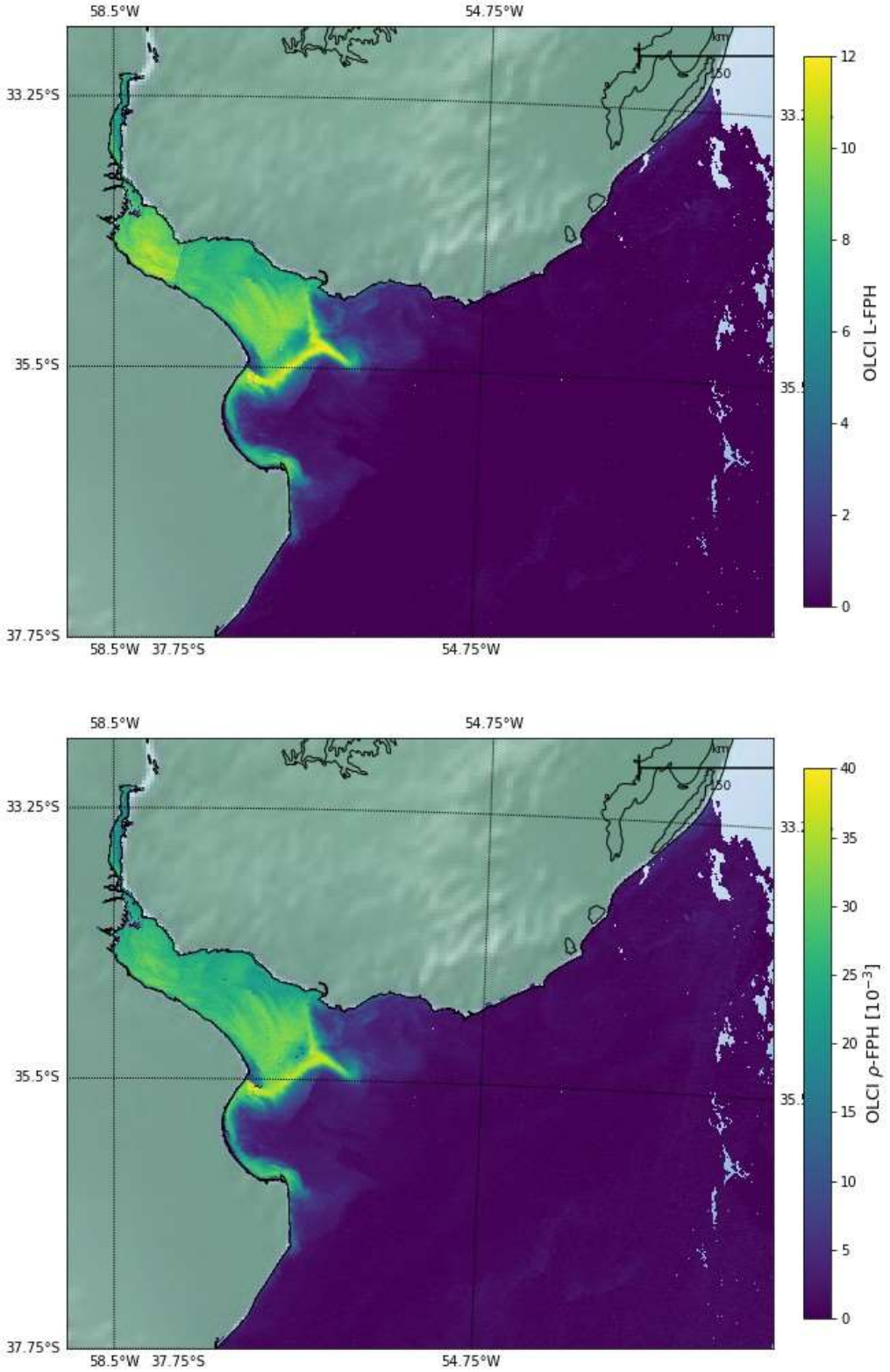


Figure 18: L-FPH (upper panel) and $\rho_w$-FPH (lower panel) at Rio de la Plata.

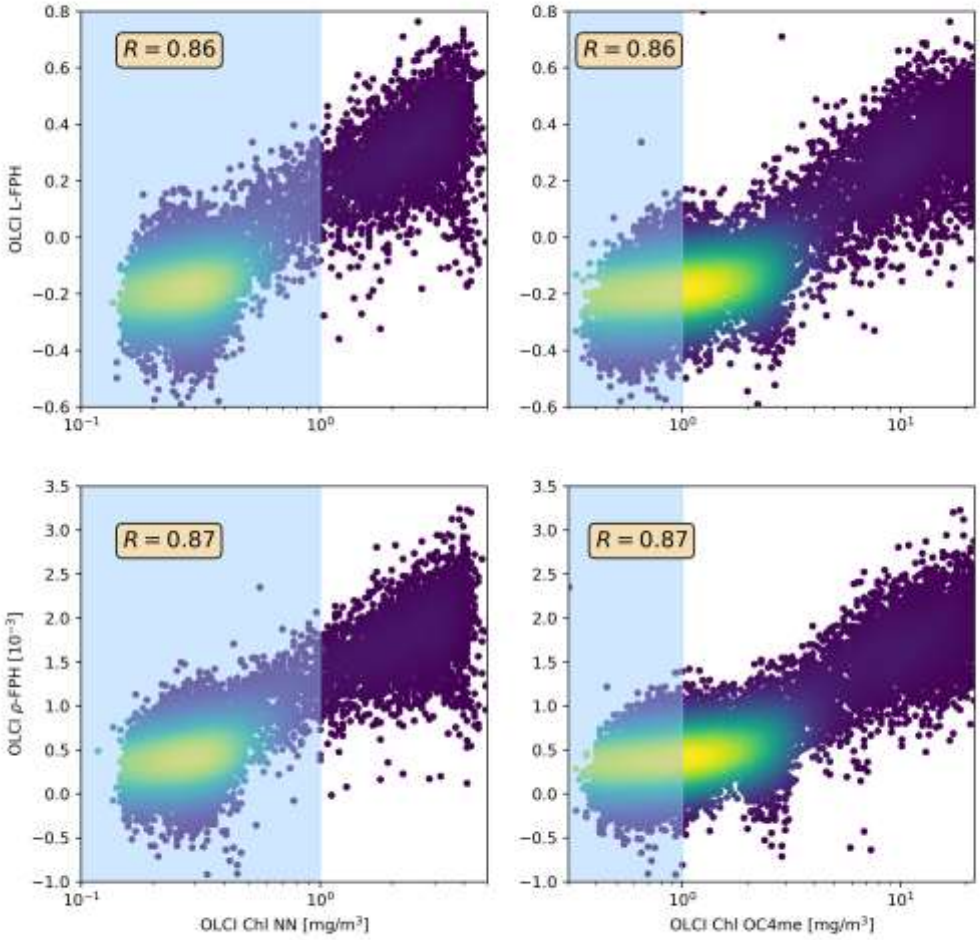


Figure 19: L-FPH and $\rho_w$-FPH against Chl from OC4Me (upper panel) and against Chl from NN in Rio de la Plata.

### 4.4.2 Black sea

The Black Sea lies between southeastern Europe and Asia Minor. Excluding its northern arm, the Sea of Azov, the Black Sea occupies about 168,500 square miles (436,400 square kilometers). It is connected to the Aegean Sea through the Bosporus, the Sea of Marmara, and the Dardanelles (https://www.ceoe.udel.edu/blacksea/geography/index.html). The Chlorophyll concentration undergoes high seasonal and annual variability. Chlorophyll as a product from the OC4Me and NN processor on the 2nd of November, 2017 is shown in Fig. 20. The concentration reaches from 0.5 $mgm^{-3}$ in the middle to 4 $mgm^{-3}$ in the shelf regions, while the main portion is below 2 $mgm^{-3}$. At the shore OC4Me chlorophyll shows probably adjacency effects. L-FPH and $\rho_w$-FPH are shown in Fig. 21 and reveal patterns similar to the chlorophyll standard products. The correlation of L-FPH and $\rho_w$-FPH to Chlorophyll from OC4Me and NN is shown in Fig. 22. The correlation coefficient R between L-FPH and Chlorophyll from NN is 0.41 and Chlorophyll from OC4Me is 0.44. The correlation coefficient R between $\rho_w$-FPH and Chlorophyll from NN is 0.43

and Chlorophyll from OC4Me is 0.45. Depending on the processor for chlorophyll most or half of the pixels are outside of the sensitivity range of the FPH product.

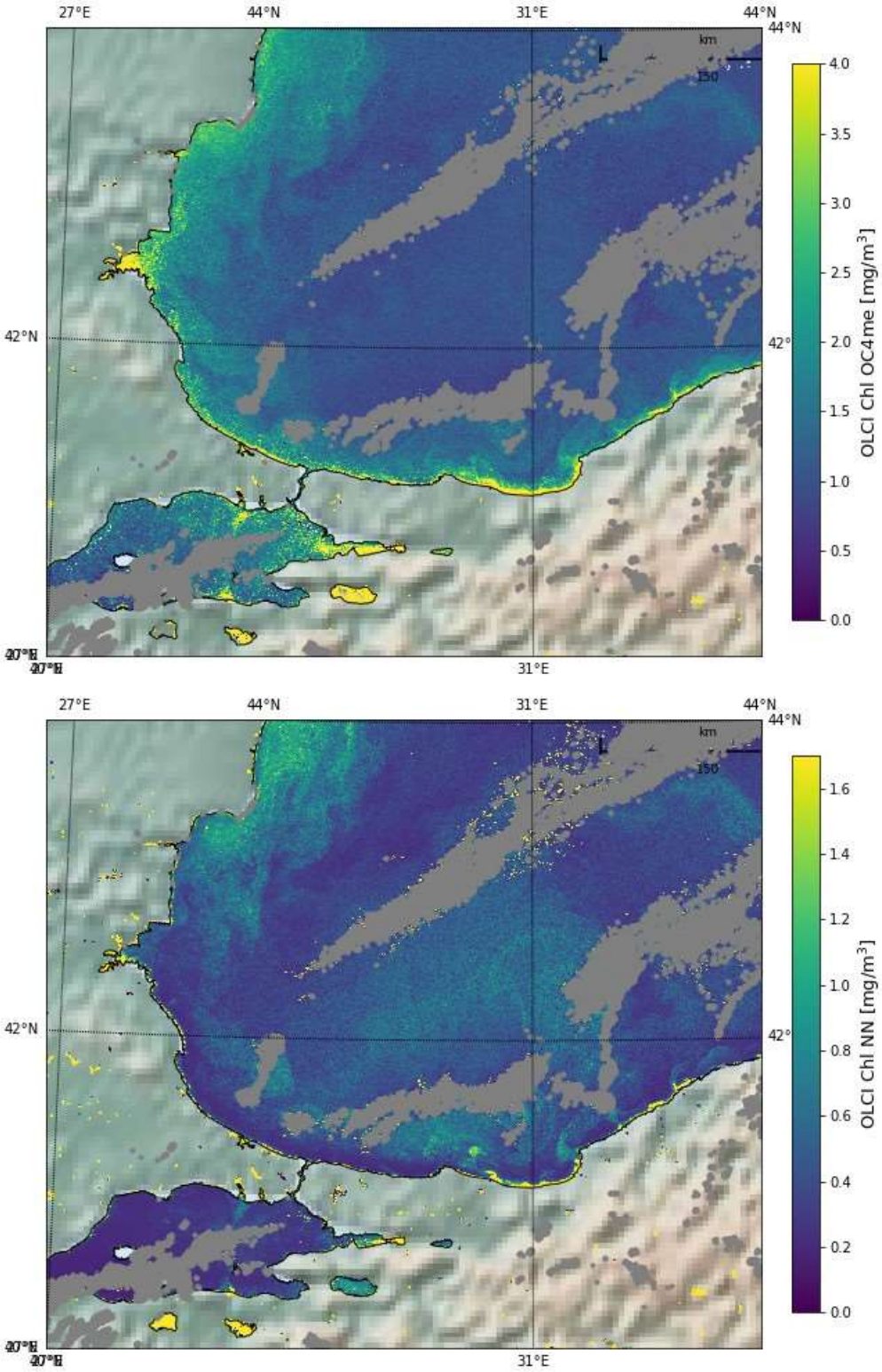


Figure 20: Chlorophyll Black Sea from OC4Me (upper panel) and Neural Net processor (lower panel)

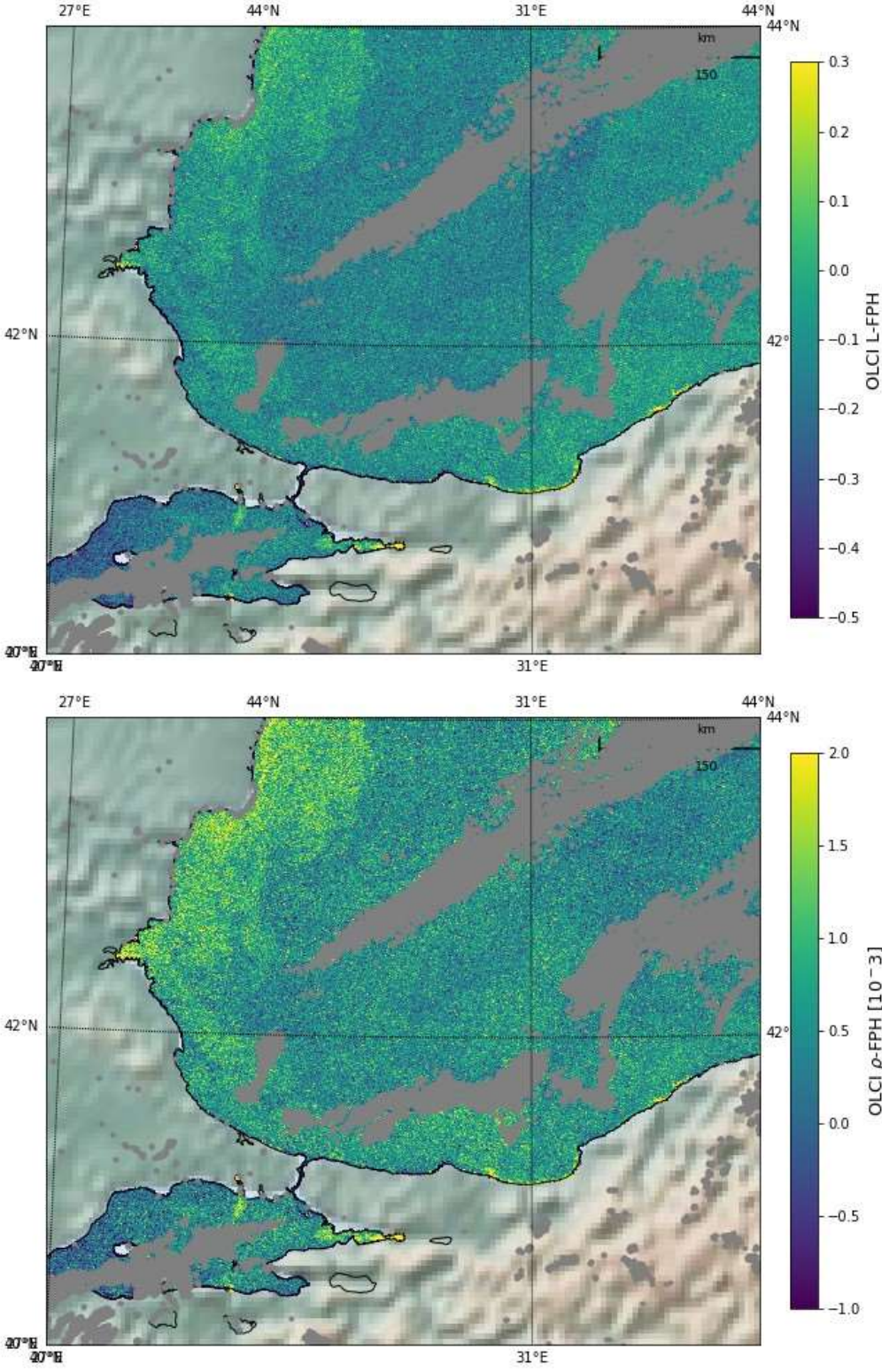


Figure 21: L-FPH (upper panel) and $\rho_w$-FPH (lower panel) in the Black Sea.

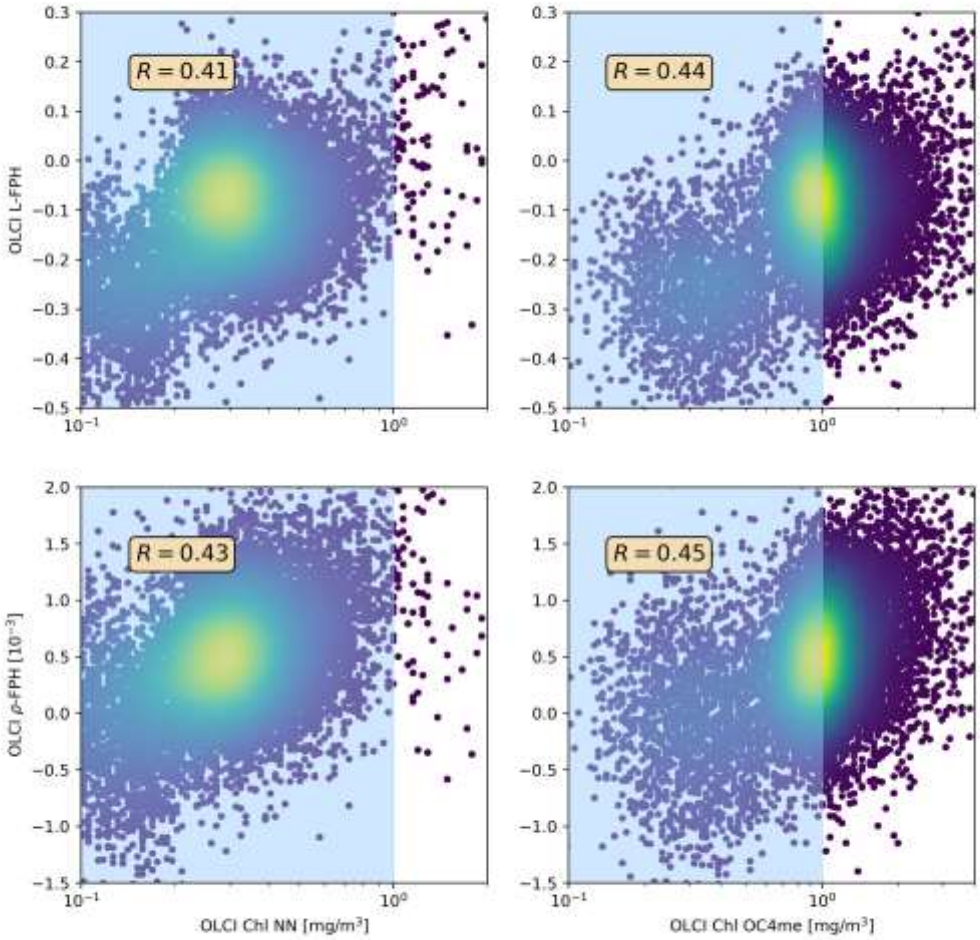


Figure 22: L−FPH and $\rho_w$−FPH against Chl from OC4me (upper panel) and against Chl from NN in the Black Sea.

### 4.4.3 Barents Sea

The Barents Sea is a marginal sea of the Arctic Ocean, located off the northern coasts of Norway and Russia and is divided between Norwegian and Russian territorial waters. It is a rather shallow shelf sea, with an average depth of 230 metres, and is an important site for both fishing and hydrocarbon exploration. Despite being part of the Arctic Ocean, the Barents Sea has been characterised as "turning into the Atlantic" because of its status as "the Arctic warming hot spot." Hydrologic changes due to global warming have led to a reduction in sea ice and in stratification of the water column, which could lead to major changes in weather in Eurasia. Due to the North Atlantic drift, the Barents Sea has a high biological production compared to other oceans of similar latitude. The spring bloom of phytoplankton can start quite early close to the ice edge, because the fresh water from the melting ice makes up a stable water layer on top of the sea water.

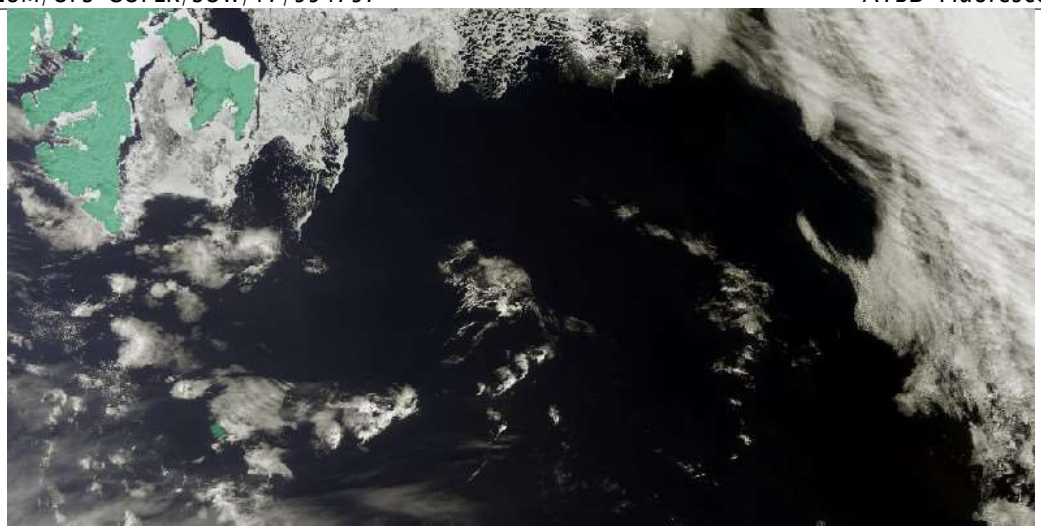

Figure 23: RGB, OLCI Level-1b, Barents Sea.

Fig. 24 and 25 show L-FPH and $\rho_w$-FPH and OC4Me and NN Chlorophyll on the 7th of May, 2018 in the Barents Sea. L-FPH and $\rho_w$-FPH reveal distinctive patterns, which are very similar to the patterns detected as NN chlorophyll. The correlation of L-FPH and $\rho_w$-FPH to Chlorophyll from OC4Me and NN is shown in Fig. 26. Both, the correlation coefficient R between L-FPH and Chlorophyll from NN and Chlorophyll from OC4Me is 0.79. The correlation coefficient R between $\rho_w$-FPH and Chlorophyll from NN is 0.76 and Chlorophyll from OC4Me is 0.80.

### 4.4.4 Conclusion on the comparison to OLCI standard chlorophyll

As well L-FPH as $\rho_w$-FPH show an overall good correlation to OC4me and NN chlorophyll above a concentration of around 1 $mg/m^3$.

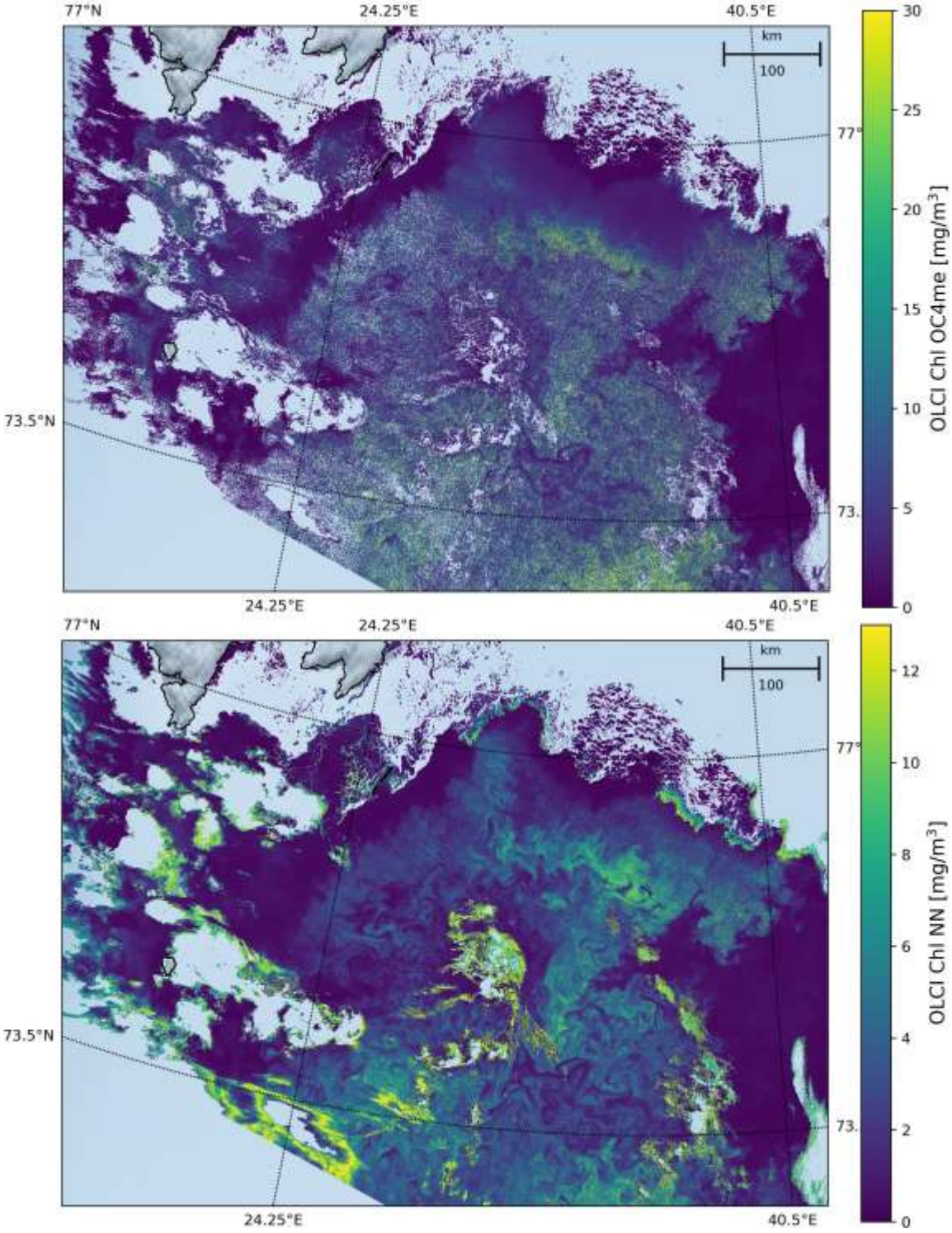


Figure 24: Chlorophyll in the Barents Sea from OC4Me (upper panel) and Neural Net processor (lower panel)

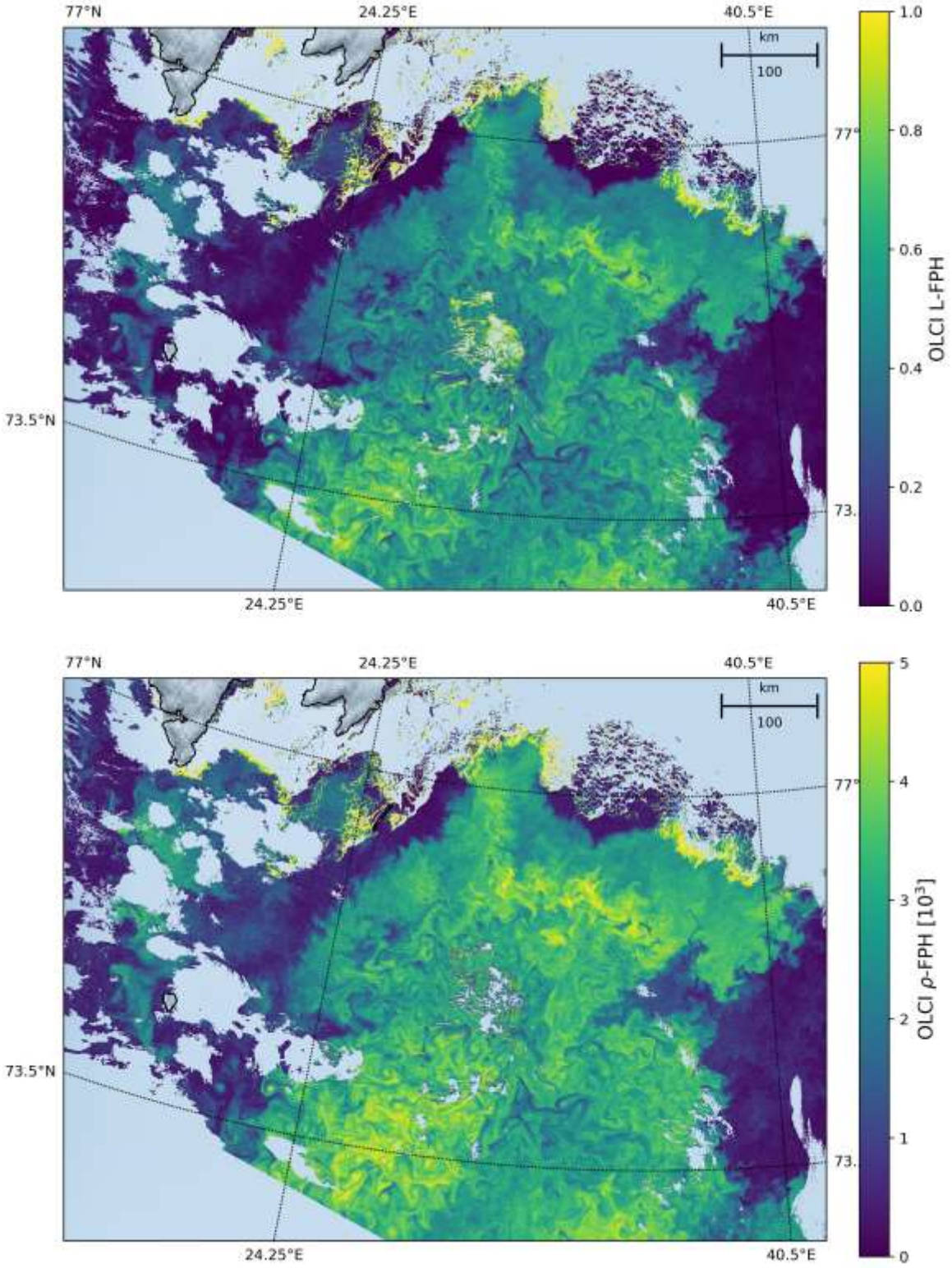


Figure 25: L-FPH (upper panel) and $\rho_w$-FPH (lower panel) in the Barents Sea.

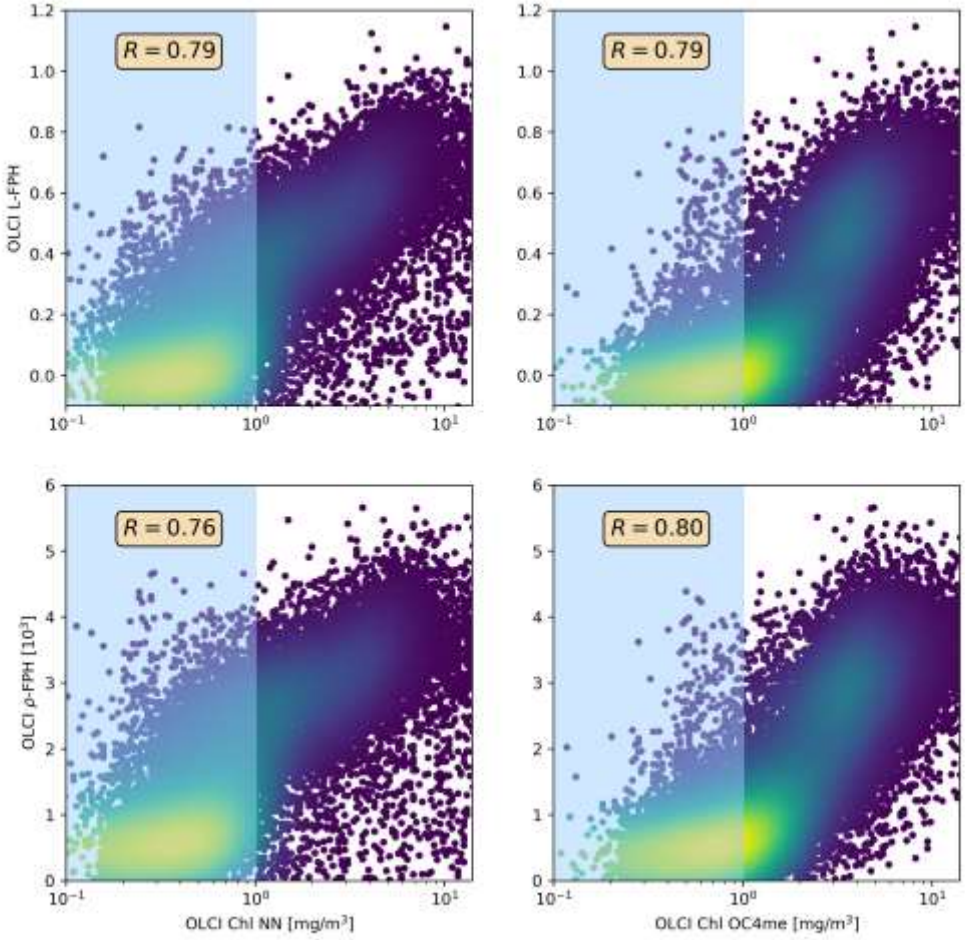


Figure 26: L-FPH and $\rho_w$-FPH against Chl from OC4me (upper panel) and against Chl from NN in the Barents Sea.

## 4.5 Validation against MODIS nFLH

nFLH from MODIS is a well-established remote sensing product and independent of our OLCI FPH products in terms of instrumental issues as well as in terms of retrieval algorithm issues. The retrieval of MODIS nFLH is described in detail in Behrenfeld et al. (2009). Note, that MODIS nFLH algorithm is based on the fully normalized water-leaving radiances, including BRDF correction, as described under Feldman, but both our OLCI products still include BRDF effects (see section 1.1.5). In the following we show three examples of a matchup comparison between OLCI and MODIS, in each case the quantitative comparison is shown in a correlation plot in Figures 29, 32 and 35 after collocation of the two, where OLCI pixels are projected on MODIS pixels. Both, MODIS nFLH and OLCI L-FPH are based on the physical radiances (the MODIS one has undergone atmospheric correction), where the spectral peak around 682 nm is expected to originate from

the ocean. Accordingly both measures are expected to be very similar in absolute values. Still differences have to be expected, because MODIS nFLH characterizes the line-height of the measured spectrum at 678 nm and OLCI FPH characterizes a peak height of a peak at 682.5 nm, which might be decreased by a dip at 673.5 nm (see the description of the two algorithms, in the ATBD section 3.3.2).

### 4.5.1 Barents Sea, 5.7.2018, OLCI-B: 9:21am, MODIS AQUA: 8:40am

The Barents Sea is described already in sec. 4.4.3. We compare MODIS AQUA nFLH and OLCI-B FPH in the Barents Sea on the 7th of May, 2018. Fig. 27 shows the footprint of the collocated measurements of MODIS and OLCI.


Figure 27: Footprint (red rectangle) of the collocated MODIS and OLCI measurements, that are compared here.

For this comparison MODIS and OLCI differ in the overpass times by about 40 min. Fig. 28 shows the MODIS nFLH, the corresponding OLCI products are shown in Fig. 25. The patterns look by eye nearly identical. Fig. 29 shows OLCI L-FPH over MODIS nFLH and OLCI $\rho_w$-FPH over MODIS nFLH in a density plot. OLCI L-FPH ranges between 0 and 0.9, with the center of density at 0.6. OLCI $\rho_w$-FPH ranges between 0 and 5, with the center of density at 3.5. MODIS nFLH ranges between 0 and 0.9, with the center of density at 0.6. The correlation coefficient between MODIS nFLH and OLCI L-FPH as well as between MODIS nFLH and OLCI $\rho_w$-FPH is R=0.81.

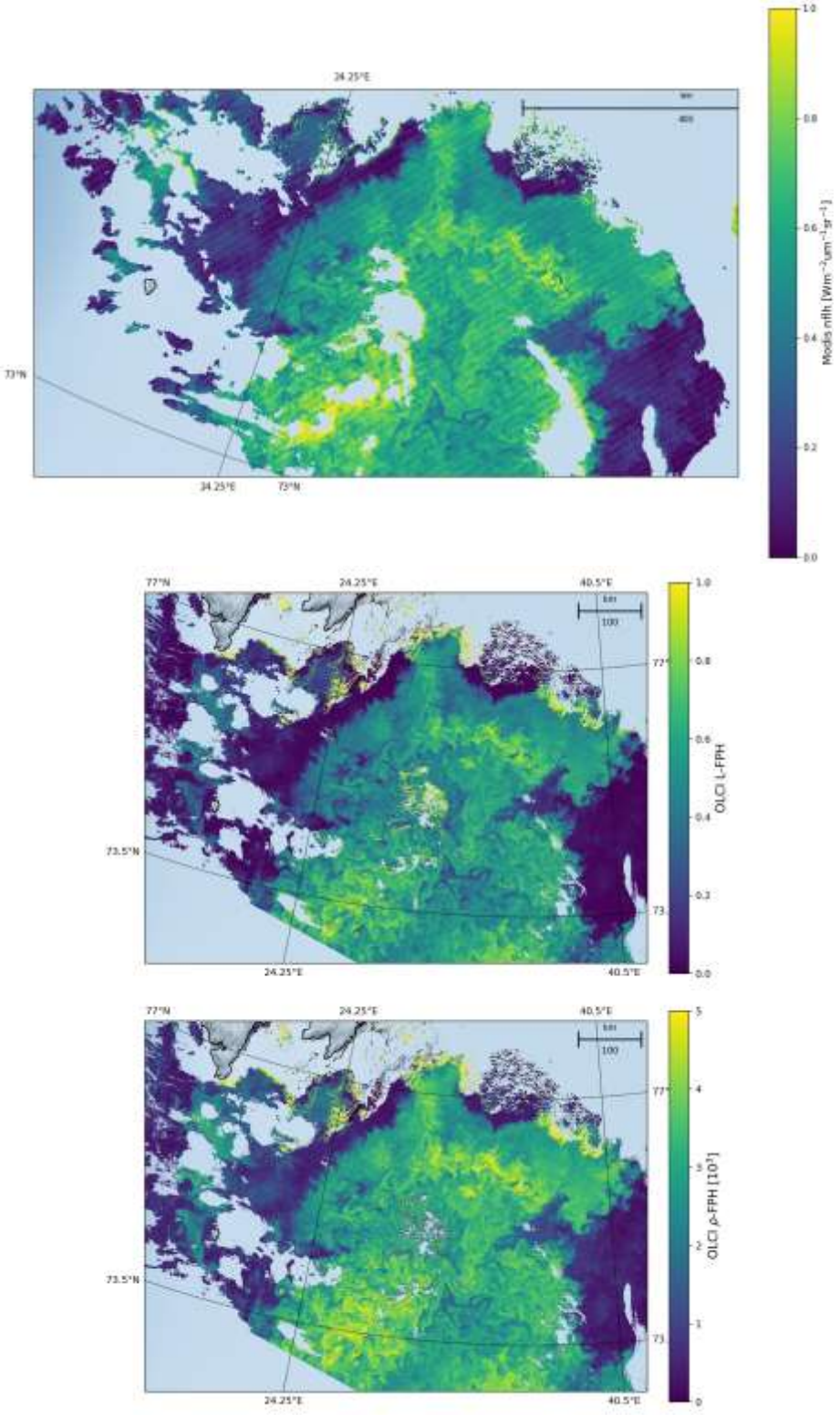


Figure 28: MODIS nFLH at 8:35-8:40 am (upper panel), OLCI L-FPH (middle panel) and $\rho_w$-FPH (lower panel) at 9:18 -9:21 am in the Barents Sea.

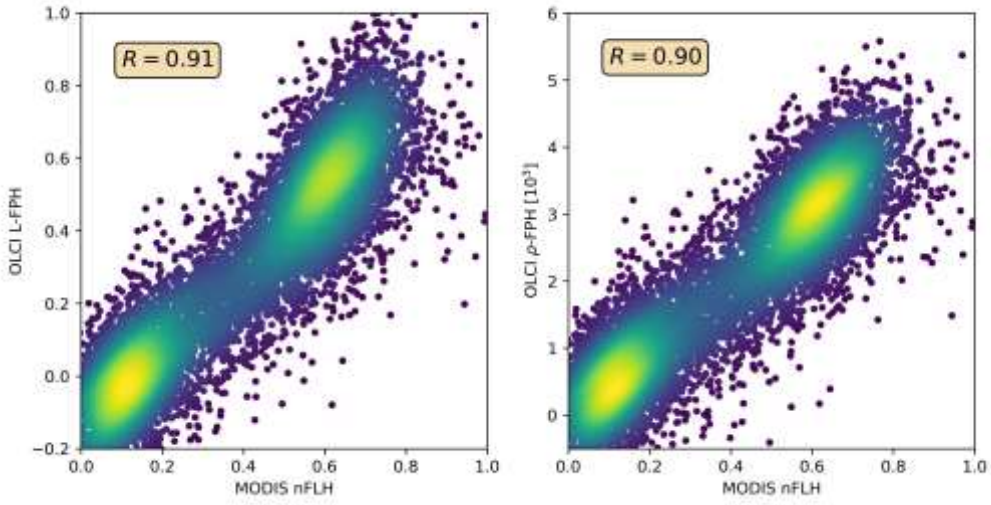


Figure 29: OLCI L-FPH over MODIS nFLH (left) and OLCI $\rho_w$-FPH over MODIS nFLH in the Barents Sea (right).

### 4.5.2 Namibian Coast, 25.11.2017, OLCI-A: 8:36am, MODIS AQUA: 12:34pm

Phytoplankton blooms are common in the coastal waters off southwest Africa where cold, nutrient- rich currents sweep north from Antarctica and interact with the coastal shelf. At the same time, the easterly trade winds push surface water away from the shore, allowing water from the ocean's floor to rise to the surface, bringing with it iron and other material (NASA, 2017). The coastal up-welling system has high seasonal and inter-annual variability in atmospheric forc- ing, in properties of water masses on the shelf offshore the Republic of Namibia, and in oxygen supply and demand on the shelf. In consequence, concentrations and ratios of nutrients in up- welling water have steep gradients in space and time (Hansen, 2014). We compare MODIS AQUA nFLH and OLCI-A FPH at the Namibian coast on the 25th of November, 2017. Fig. 30 shows the footprint of the collocated measurements of MODIS and OLCI.

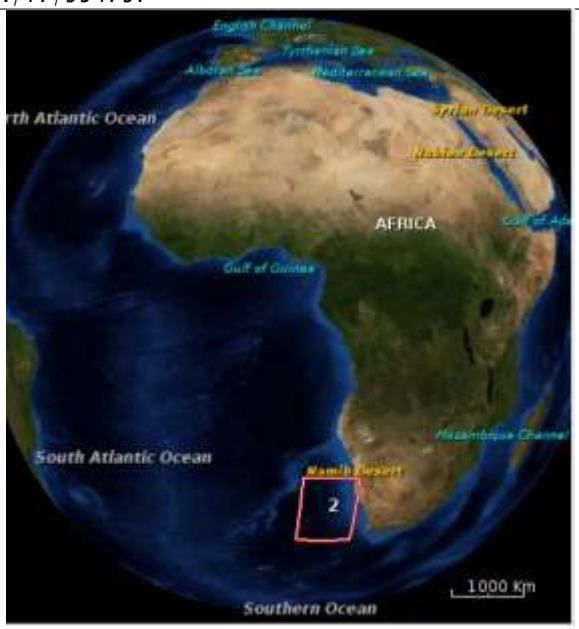


Figure 30: Footprint (red rectangle) of the collocated MODIS and OLCI measurements, that are compared here.

For this comparison MODIS and OLCI differ in the overpass times by about 4 h. Fig. 31 shows OLCI L-FPH, OLCI $\rho_w$-FPH and MODIS nFLH. The main patterns look similar, but the relations in concentration from one feature to another are a bit different. Fig. 32 shows OLCI L-FPH over MODIS nFLH and OLCI $\rho_w$-FPH over MODIS nFLH in a density plot. There are two centers of density. OLCI L-FPH ranges between -0.6 and 0.3, with the center of density at -0.3 and -0.1. OLCI $\rho_w$-FPH ranges between -0.4 and 1.5, with the center of density at 0.4 and 0.8. MODIS nFLH ranges between 0 and 0.4, with the center of density at 0.1 and 0.2. The correlation coefficient between MODIS nFLH and OLCI L-FPH is R=0.54 and between MODIS nFLH and OLCI $\rho_w$-FPH R=0.50.

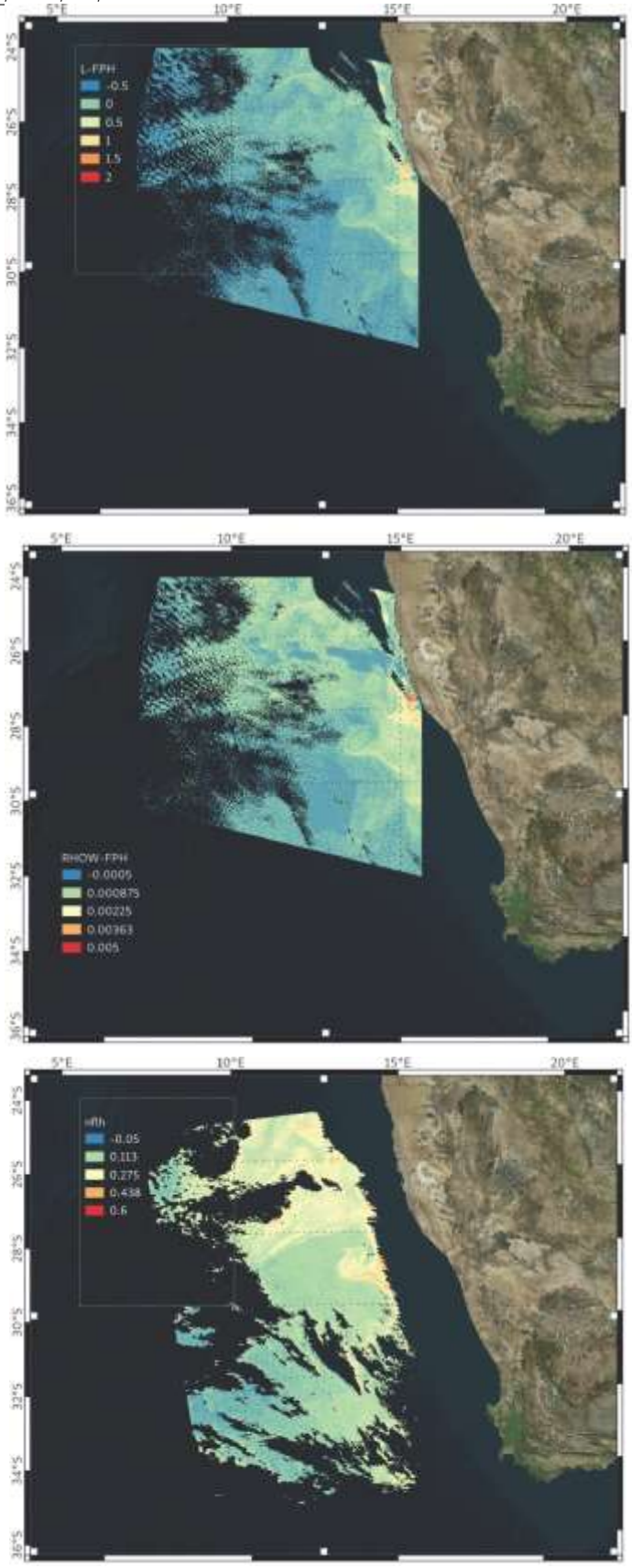


Figure 31: Upper panel: OLCI L-FPH, middle panel: OLCI Pw-FPH, lower panel: MODIS nFLH near the Namibian coast.

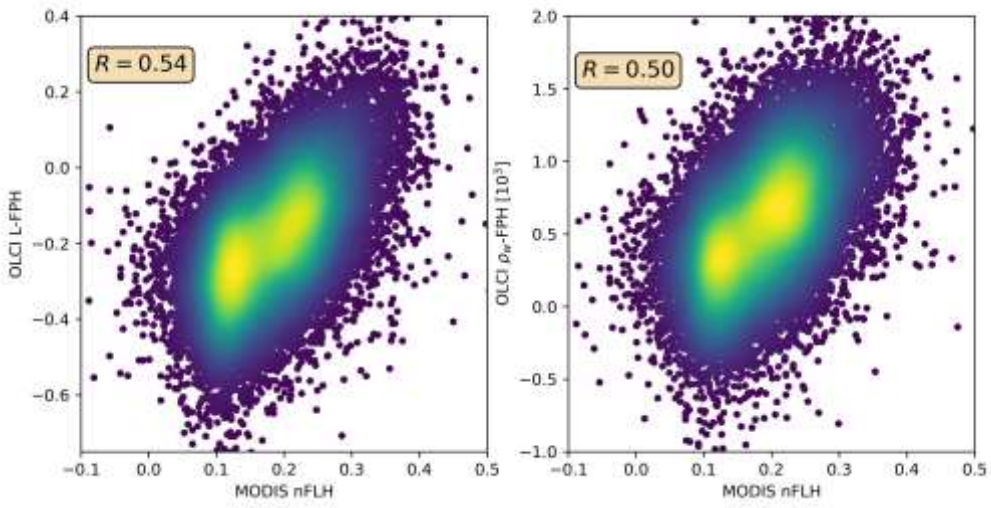


Figure 32: OLCI L-FPH over MODIS nFLH (left) and OLCI $\rho_w$-FPH over MODIS nFLH near the Namibian coast.

### 4.5.3 German Bight, 26.8.2019, OLCI-A: 10:27am, MODIS AQUA: 12:13pm

The German Bight is the southeastern bight of the North Sea bounded by the Netherlands and Germany to the south, and Denmark and Germany to the east. Several main rivers discharge into the southern North Sea, such as the river Elbe, the river Rhine, the river Weser and the river Ems. The position of the estuaries of these rivers, along with the counterclockwise residual current pattern which carries riverborne substances from west to east, favour the accumulation of eutrophying substances in the German Bight. Its coastal zone plays a major role as a recipient of large amounts of nutrient from human activities, including effluents, agriculture runoff, and municipal sewage (Schlüter, 2010). We compare MODIS AQUA nFLH and OLCI-A FPH in the German Bight on the 26th of August, 2019. Fig. 33 shows the footprint of the collocated measurements of MODIS and OLCI. For this comparison MODIS and OLCI differ in the overpass times by about

Figure 33: Footprint (red rectangle) of the collocated MODIS and OLCI measurements, that are compared here.

2 h. Fig. 34 shows OLCI L-FPH, OLCI $\rho_w$-FPH and MODIS nFLH. The patterns look nearly identical. Fig. 35 shows OLCI L-FPH over MODIS nFLH and OLCI $\rho_w$-FPH over MODIS nFLH in a density plot. OLCI L-FPH ranges between -0.35 and 0.1, with the center of density at -0.2. OLCI $\rho_w$-FPH ranges between -0.25 and 1, with the center of density at 0.1. MODIS nFLH ranges between -0.05 and 0.2, with the center of density at 0.03. The correlation coefficient between MODIS nFLH and OLCI L-FPH is R=0.84 and between MODIS nFLH and OLCI $\rho_w$-FPH R=0.87.

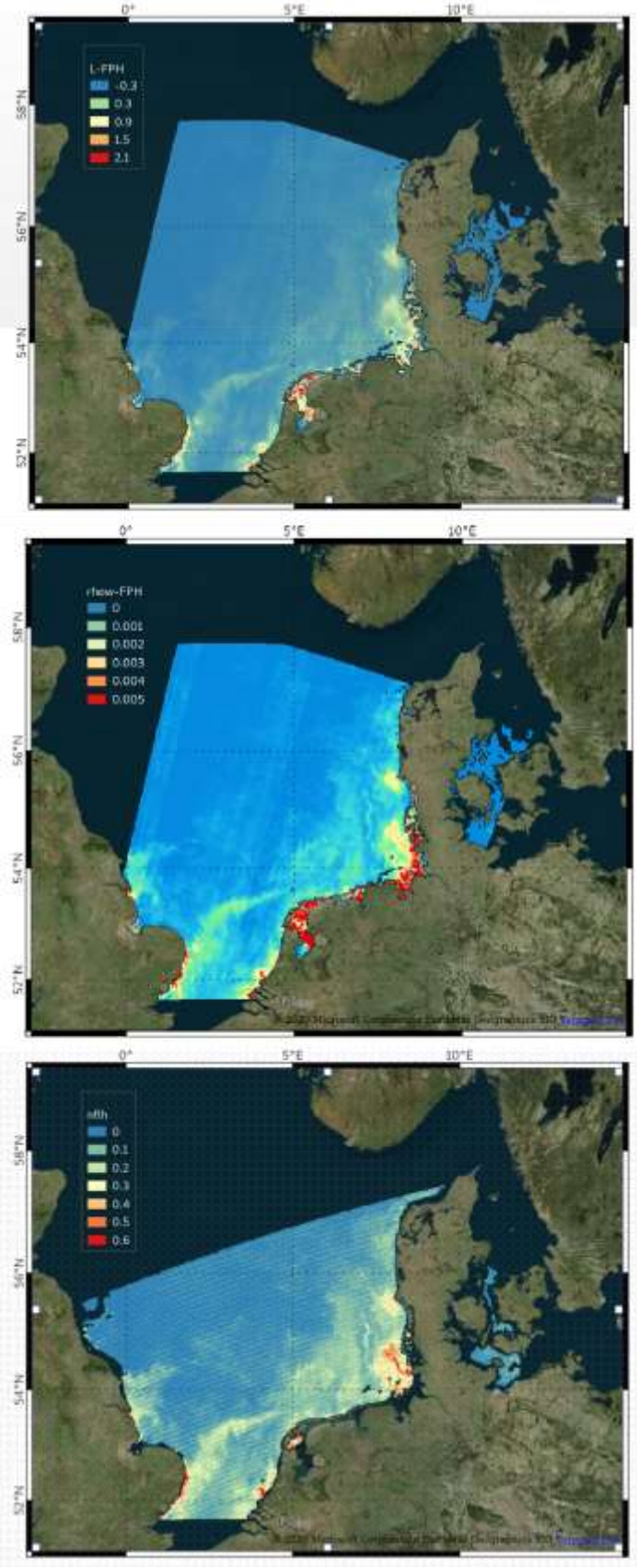


Figure 34: Upper panel: OLCI L-FPH, middle panel: OLCI $\rho_w$-FPH, lower panel: MODIS nFLH in the German Bight.

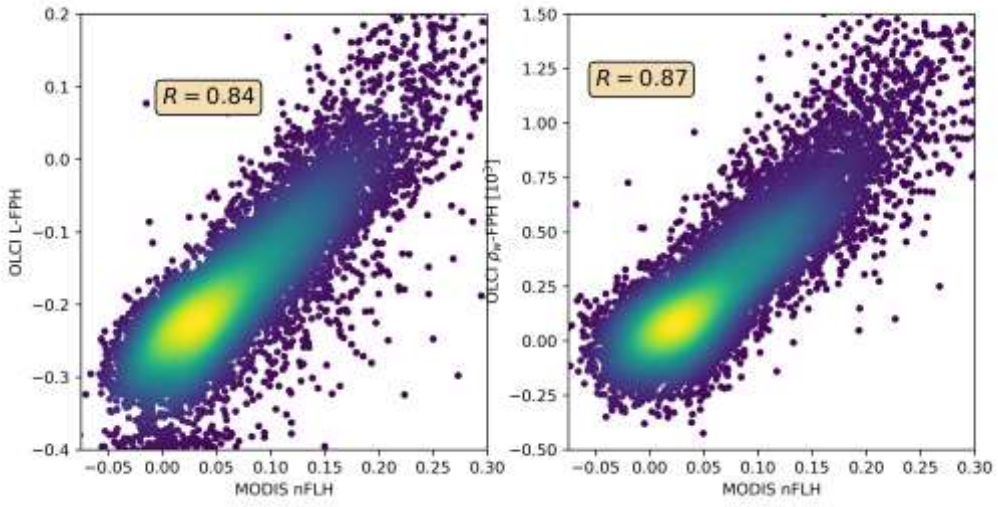


Figure 35: OLCI L-FPH over MODIS nFLH (left) and OLCI $\rho_w$-FPH over MODIS nFLH for the German Bight.

### 4.5.4 Conclusion on the comparison to MODIS nFLH

The overall patterns of OLCI L-FPH and $\rho_w$-FPH are so alike that the correlation coefficient to MODIS is in both cases nearly the same. Due to the physical units, absolute values of L-FPH are more comparable to MODIS, than the ones of $\rho_w$-FPH, while the negative offset of $\rho_w$-FPH is more comparable to MODIS, than the one from L-FPH. This is most likely due to the atmospheric correction, which is applied as well to MODIS nLw as to OLCI $\rho_w$. The correlation is very good for the Barents Sea and the German Bight example and less good for the Namibian coast, where the time gap of 4h is probably too large.

## 4.6 Validation on simulated data

Radiative transfer simulations are performed for developing and testing the OC-Fluo algorithm. As described before in section 4.1 the emitted fluorescence quantum in nature depends on many factors, like the quantum yield, the chlorophyll concentration, illumination, etc., which are not known, or at least not accurately known. A synthetic approach, like the one described here is the only way to control all influences on the fluorescence signal. In the RTM fluorescence is a strictly increasing function of the chlorophyll concentration. In case the mathematical function is able to capture the fluorescence peak from OLCI spectrally convoluted reflectances the retrieved FPH should be a strictly increasing function to input chlorophyll.

### 4.6.1 The RTM MOMO and the bio-optical model

The simulations are performed using the vector version of MOMO (Fell and Fischer (2001), Hollstein and Fischer (2012)). Here a horizontal homogeneous atmosphere and ocean consisting of layers with vertical uniform optical properties are assumed. The upward and downward directed light field is calculated at all inter layer boundaries and for all solar positions. The azimuthal dependence of the light field is internally expressed as Fourier series and reconstructed at equidistant distributed azimuth angles. The model is operated by several input files which govern the height profile of atmosphere and ocean, the scatterers, the absorbers and the at-

mosphere ocean interface. For this set of simulations a water body was implemented with 20 layers of 1 m thickness and is assumed to be homogeneous with an equal distribution of constituents (phytoplankton and CDOM) in each layer. The absorption coefficient of pure sea water

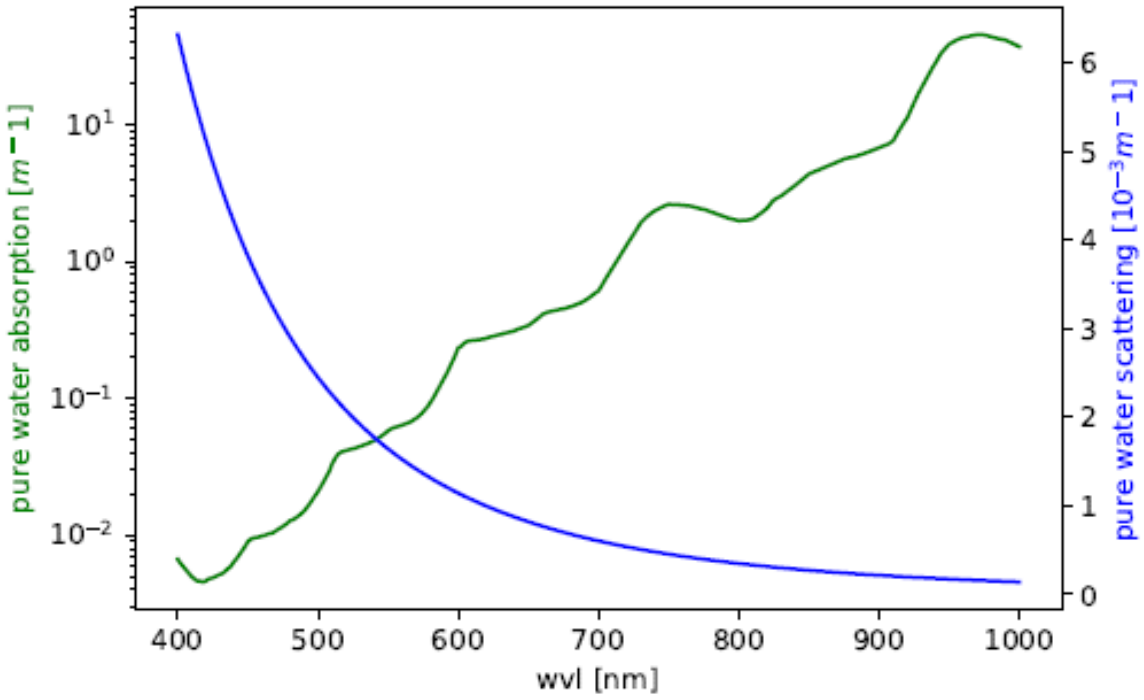


Figure 36: Spectral scattering (blue) and absorption (green) of pure seawater for salinity S=20 PSU and temperature T=20 °C (Röttgers et al., 2010).

Table 5: Input IOPS for MOMO

| IOP [1/m] | 0.04 | 0.4 | 0.8 | 1.0 | 1.4 | 1.8 | 3.0 | 5.0 | 7.0 |
|---|---|---|---|---|---|---|---|---|---|
| concentration [mg/m$^3$] | 0.84 | 8.4 | 16.8 | 21 | 29.4 | 37.8 | 63 | 105 | 147 |

(see Fig. 36) is a result from the ESA project WATERRADIANCE (Röttgers et al., 2010) as a linear expansion with coefficients for salinity and temperature. The volume scattering coefficient of sea water is the sum of contributions from density fluctuations and concentration fluctuations and has been discussed in Zhang and Hu (2009). Fig. 36 shows the absorption and scattering coefficients for salinity S=20 PSU and temperature T=20 °C. We apply a bio-optical model, where chlorophyll concentration governs as well chlorophyll absorption coupled to chlorophyll fluorescence with a quantum yield of 0.03, as CDOM absorption and scattering (Bricaud et al. (2010)). The chlorophyll-a extinction coefficient and the corresponding single scattering albedo control the amplitude and spectral signature of phytoplankton. A normalized chlorophyll-a absorption spectrum is scaled at 440 nm in order to calculate the absorption spectrum $a_{ph}(\lambda)$ for different phytoplankton amounts. The single scattering albedo $\omega_0$ at 440 nm is set to 0.68 (J. Fischer, pers. communication) to calculate spectral phytoplankton scattering $b_{ph}(\lambda)$ with

$$b_{ph}(\lambda) = a_{ph}\omega_0\lambda/(1-\omega_0) \quad (19)$$

Phytoplankton scattering is constrained by a phase function measured from Petzold (1972) which can be mathematically expressed with the Fournier-Forand function with a backscattering ratio of 0.01986. The simulated data cover a large range of chlorophyll concentrations (see table 5), which are governed by the absorption coefficients at 440 nm from 0.004 $m^{-1}$ to 7 $m^{-1}$. The simulations are performed in 1 nm resolution from 390 nm to 740 nm.

Technically the fluorescence is simulated in two subsequent model runs. In the first run the energy that is absorbed by chlorophyll (photosynthetically active radiation, PAR) is calculated and in the second model run this energy is multiplied by the quantum efficiency of 0.03 and implemented as a Gaussian shaped peak source, centered at 682.5 nm and halfwidth of 25 nm.

### 4.6.2 Calculation of $\rho_w$ and convolution to OLCI and MERIS spectral response function

The $\rho_w$ is not a direct model output, but is derived from up- and downward radiances ($L\uparrow, L\downarrow$) and irradiances ($E\uparrow, E\downarrow$) just above water surface:

$$\rho_w(\theta, \phi, \lambda) = \pi L_w(\theta, \phi, \lambda)/E\downarrow(\lambda) \tag{20}$$

where the water-leaving radiance $L_w$ is calculated from

$$L_w(\theta, \phi, \lambda) = (L\uparrow(\theta, \phi, \lambda) - L_{black}(\theta, \phi, \lambda))/E\downarrow(\lambda) \tag{21}$$

and $L_{black}$ is $L\uparrow$ from only the ocean surface. This is realised in the model, by implementing a very thin water body with a black surface below.

The resulting $\rho_w$ is shown in Fig. 37 in 1 nm resolution and in OLCI's spectral resolution within the spectral domain of the OLCI bands Oa8 to Oa12. The MERIS band setting, which is a subset of OLCI's bands is included.

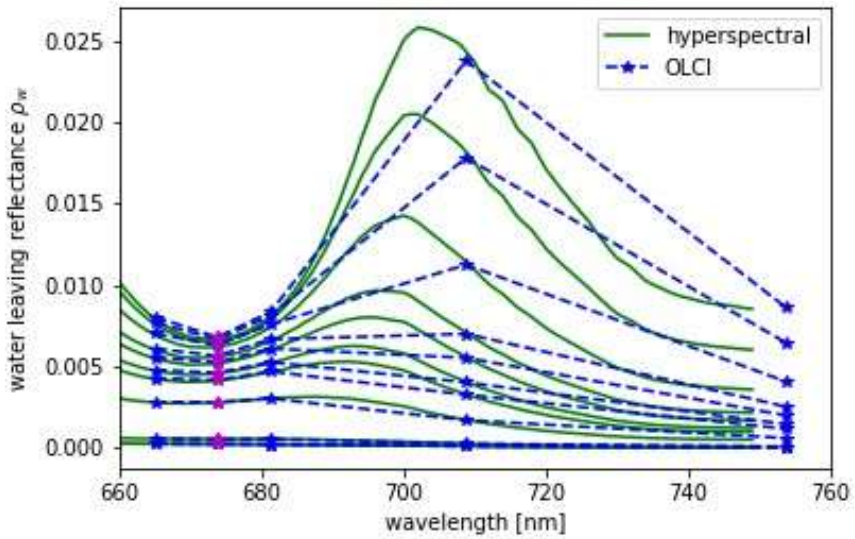


Figure 37: Hyperspectral (green) $\rho_w$ from RTM and its convolution to OLCI (blue) spectral resolution for $\theta_S$=48°, $\theta_V$=34°, $\phi_V$=90° and chlorophyll concentrations given in table 5, while the lowest spectrum is the one with the lowest chlorophyll concentration. Band Oa09 from OLCI which is additional to MERIS bands is shown in magenta.

We apply the proposed algorithm to the convoluted remote sensing reflectances. The upper

panel in Fig. 38 shows $\rho_w$-FPH retrieved from synthetic spectra over Chl, calculated from the simulations input. Results are shown for OLCI and MERIS band setting, while the MERIS results are produced by just excluding band Oa9 from the retrieval. Both band settings give an unambigous and very similar relationship. The lower panel in Fig. 38 shows the relative difference of $\rho_w$-FPH retrieved from synthetic spectra in OLCI and MERIS band setting over chlorophyll. Up to 40mg/m³ chlorophyll the difference is less than 4% and even for very high concentrations up to 140mg/m³ it does not exceed 10%. This means the algorithm can be also applied to MERIS measurements and the results can be directly compared to each other. Consequently long time series of nearly twenty years of FPH could be generated and analysed. In order to investigate the reasons for the similarity of OLCI and MERIS results, we illustrate the extracted spectral components. The division into the spectral components is shown in Fig. 39 for OLCI and for only MERIS bands applied to a $\rho_w$-spectrum with low and with high chlorophyll. For low chlorophyll concentrations the spectral model seems to reproduce the simulated spectrum perfectly

as well for MERIS as for the OLCI band setting. For higher concentrations the additional band Oa9 pulls the reproduced spectrum a bit down, which leads to a slightly lower FPH. The fact that the reproduced spectrum is slightly off the measured bands indicates that for extremely high chlorophyll concentrations the model could be adjusted to a spectrally even more complex behaviour.

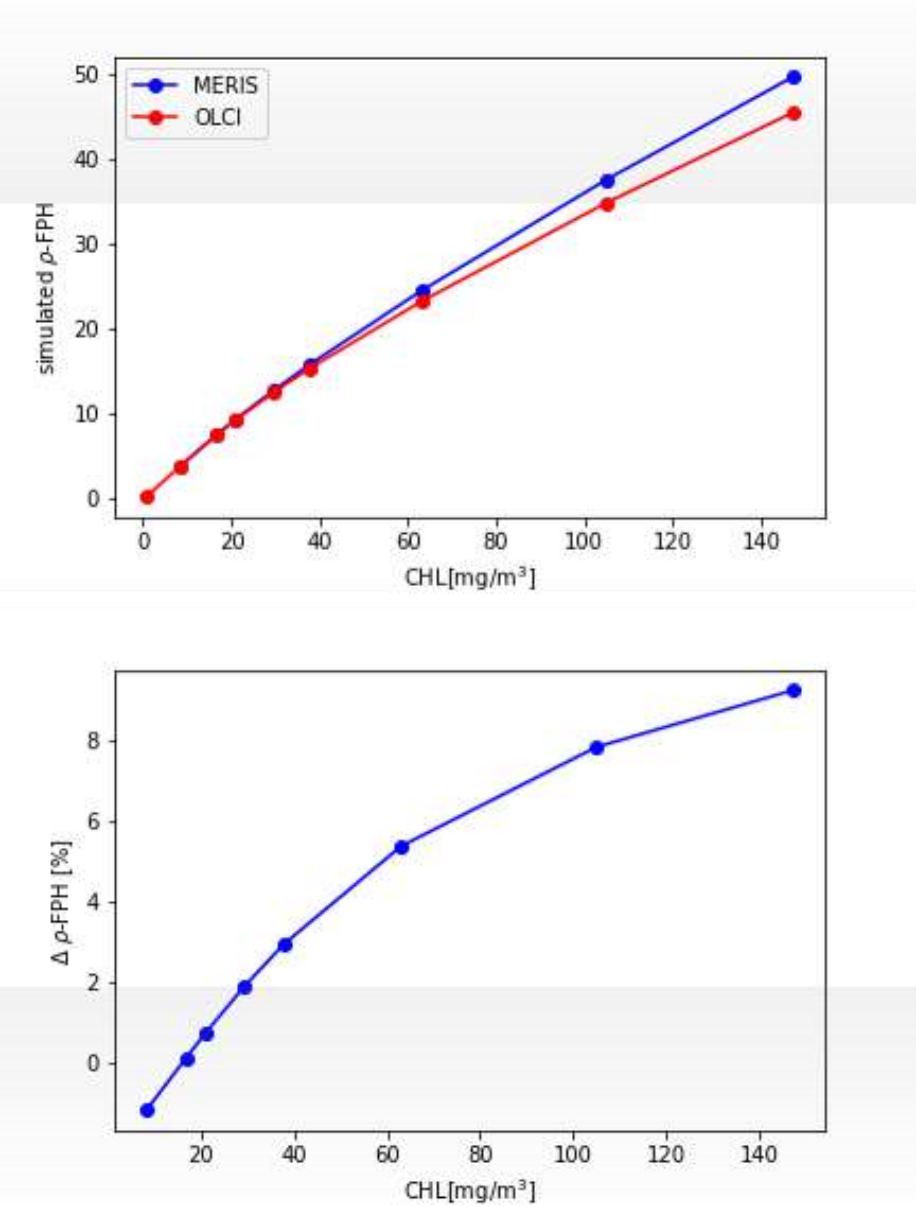


Figure 38: $\rho_w$–FPH retrieved from synthetic spectra over chlorophyll, which was input for the RTM for OLCI (red) and for MERIS (blue) band setting (upper panel). Relative difference between $\rho_w$–FPH retrieved from synthetic spectra in OLCI and MERIS band setting over chlorophyll (lower panel).

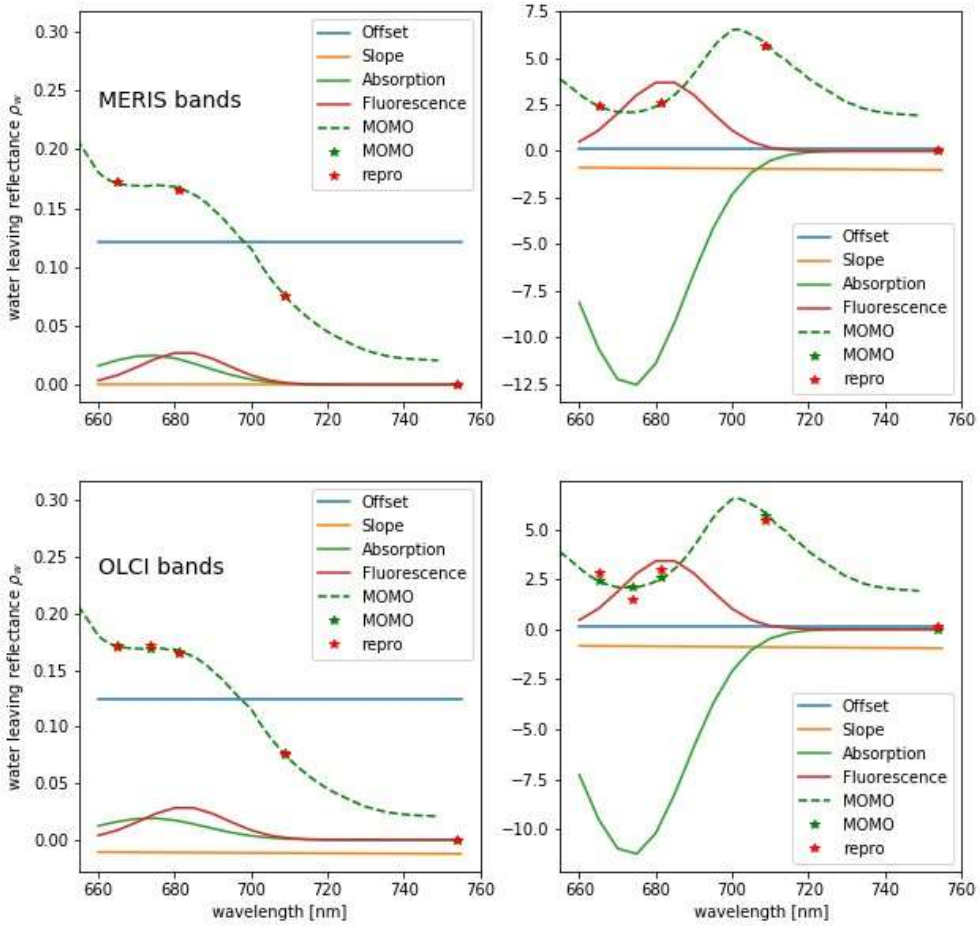


Figure 39: Components found by the retrieval of $\rho_w$-FPH applied to a $\rho_w$-spectrum with low (left panels) and with high (right panels) chlorophyll for MERIS (upper panel) and for OLCI (lower panel) band setting.

### 4.6.3 BRDF effect

In order to investigate the impact of the non lambertian BRDF of the sea surface on the Fluorescence product, we calculate from RTM the exactly normalized water-leaving reflectance $\rho_w^N$, which is $\rho_w(\theta_S, \theta_V, \lambda)$ with $\theta_S = 0$ and $\theta_V = 0$. (see sec. 1.1.5) through:

$$\rho_w(0, 0, \lambda) = \pi L_w(0, 0, \lambda)/E \downarrow (\lambda) \tag{22}$$

The water-leaving radiance $L_w$ is calculated from the difference of the upward radiance just above the surface of the modeled water body and the same quantity above a black (non-reflective) water body. This step removes the reflection at the water surface.

$$L_w(0, 0, \lambda) = (L \uparrow (0, 0, \lambda) - L_{black}(0, 0, \lambda))/E \downarrow (\lambda) \tag{23}$$

Fig. 40 shows $\rho_w^N$ (solid) and $\rho_w(\theta_S, \theta_V, \lambda)$ with $\theta_S = 48^\circ$, $\theta_V = 34^\circ$, $\phi_V = 90^\circ$ (dashed) for the different chlorophyll concentrations given in table 5 (different colours). There is a about 0.05 offset be-

tween both geometries, while the exactly normalized $\rho_w$ is brighter. This offset can be captured in the retrieval by the fitted offset. However the peak height is larger for the not normalized spectrum.

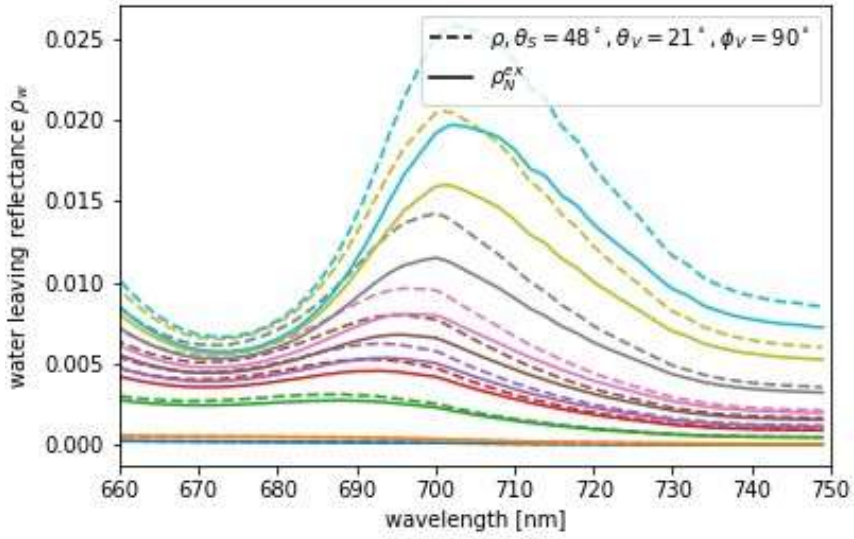


Figure 40: Hyperspectral $\rho_w^N$ (solid) and $\rho_w(\theta_S, \theta_V, \lambda)$ with $\theta_S = 48^\circ$, $\theta_V = 34^\circ$, $\phi_V = 90^\circ$ (dashed) for the different chlorophyll concentrations given in table 5 (different colours).

From the simulated $\rho_w$, $\rho_w$-FPH is retrieved for both geometries. The results are shown in Fig. 42. The relative difference is shown in Fig. 41 and gets stronger with increasing chlorophyll concentration. It exceeds 20% for the highest chlorophyll concentration (147 mg/m$^3$). For moderate chlorophyll concentrations the relative difference is around 16%.

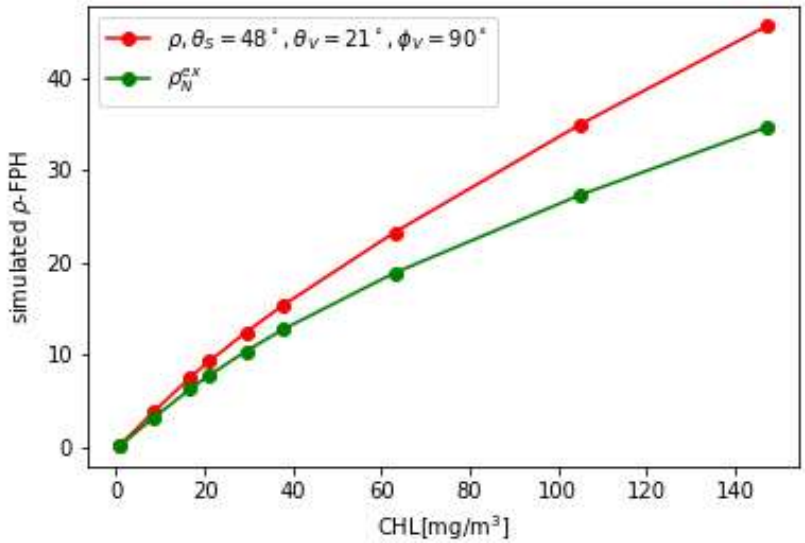


Figure 41: $\rho_w$-FPH retrieved from OLCI-resolved synthetic spectra in nadir-nadir geometry (green) and for $\theta_S = 48^\circ$, $\theta_V = 34^\circ$, $\phi_V = 90^\circ$ over chlorophyll, which was input for the RTM.

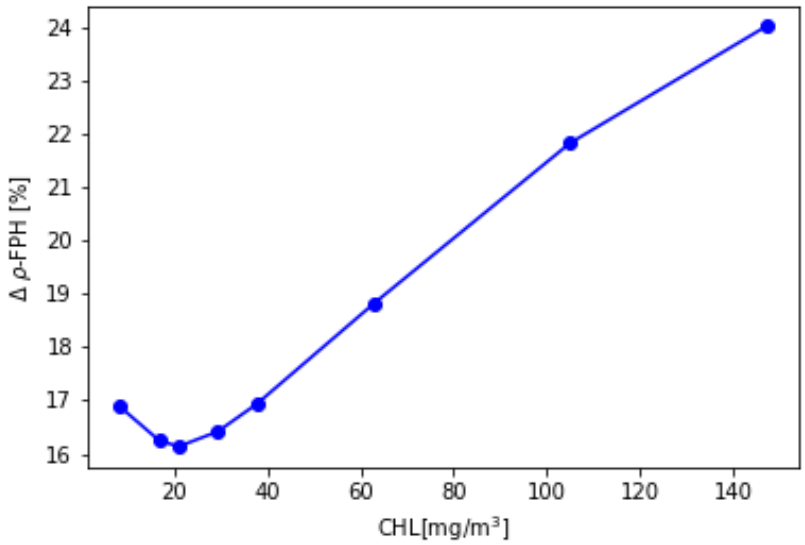


Figure 42: Relative difference between $\rho_w$-FPH from retrieved from $\rho_w(\theta_S, \theta_V, \lambda)$ with $\theta_S = 48^\circ$, $\theta_V = 34^\circ$, $\phi_V = 90^\circ$ and $\rho^w$ over chlorophyll.

### 4.6.4 Conclusion on FPH simulations

With RTM we produce spectrally high resolved $\rho_w$ spectra that are convoluted to OLCI spectral resolution and analyzed by the OC-Fluo algorithm. The resulting $\rho_w$ -FPH is a strictly increasing function of the input chlorophyll, which is governing the fluorescence in the model. From this we conclude, that FPH is a good measure of the fluorescence. Furthermore the resulting relationship between FPH and chlorophyll produced from MERIS band setting is very similar, with a difference below 10% throughout the concentration range. Therefore the algorithm is applicable to MERIS measurements and results are directly transferable. With our RTM we also studied the effect of the BRDF on the retrieved FPH. The relative difference between different viewing geometries exceeds 20% for high chlorophyll concentrations.

## 4.7 Sensitivity range of the Product

The sensitivity range of the algorithm is determined by the sensitivity of the measurements towards the fluorescence signal and the ability of algorithm to retrieve it. From our fluorescence to chlorophyll comparisons and in agreement with earlier assessments (see section 1.3), we estimate the sensitivity range of the processor to chlorophyll $> 1\,mg/m^3$ which corresponds to L-FPH $> 0$ and $\rho_w$-FPH $> 0.1$.

# 5 Conclusions on the Validation

To validate the OLCI L-FPH and $\rho_w$-FPH product we followed different approaches. Both products show a good correlation to in-situ measured and remotely sensed chlorophyll, if the chlorophyll concentration is higher than $1\,mg/m^3$. For lower chlorophyll concentrations the scatter is large and especially L-FPH values become negative. From this we can conclude, that

our FPH product is a good tracer for chlorophyll and especially for high values therein. This feature has to be studied in more detail, in particular atmospheric impacts, even when there are small their might have an impact on small fluorescence signals.

Even though OLCI FPH and MODIS nFLH are not exactly the same measures, there is a very high correlation between both.

From RTM we can conclude, that FPH is a strictly increasing function of the fluorescence magnitude. Furthermore the algorithm is applicable to MERIS measurements and results are directly transferable. With relative differences up to 20% for high chlorophyll concentrations, the BRDF effect is an open issue.

# 6 Conversion of the Fluorescence Signal to Chlorophyll

The retrieved Fluorescence signal can be converted to chlorophyll using an empirical relationship. The relationship is deduced from the global validation in section 4.2 (see Figure 10) through a polynomial fit. Technically L-FPH is converted to $\rho_w$-FPH by a polynomial fit of first degree:

$$\rho_w\text{-FPH} = 0.0047 + 0.000428519665 * \text{L-FPH} \tag{24}$$

Then $\rho_w$-FPH from L-FPH and the originally retrieved $\rho_w$-FPH are converted to chlorophyll [mg/m$^3$] by a polynomial fit of 3rd degree. The formula for the conversion to chlorophyll:

$$0.0363730393 + 303.629698 * \rho_w\text{-FPH} + 150783.567 * \rho_w\text{-FPH}^2 + -2207582.65 * \rho_w\text{-FPH}^3 \tag{25}$$

The conversion is included in the processor and the products are L-Chl and $\rho_w$-chl.

# 7 Transferability to MERIS data

From RTM we can conclude, that MERIS band setting is sufficient to be input to the presented algorithm. This is also tested with real measurements. Figure 43 shows L-FPH retrieved from OLCI measurements over L-FPH retrieved from MERIS measurements and the same for $\rho_w$-FPH. The correlation is very high and shows that the algorithm could be directly transferred to MERIS data.

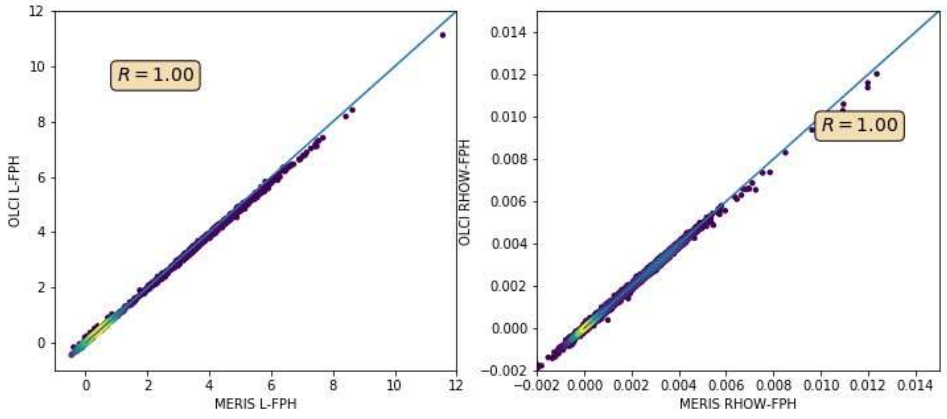


Figure 43: L-FPH retrieved from OLCI measurements over L-FPH retrieved from MERIS measurements (left panel). Same for $\rho_w$-FPH (right panel)

# 8 Algorithm assumptions

## 8.1 Scientific Assumptions

- The algorithm is based on OLCI TOA-L or $\rho_w$, which are both not normalized with respect to viewing geometry (see section 1.1.5 and section 4.6)
- The algorithm also assumes that very simple functions, the Gaussian functions, offset and slope (see section 3.3), can capture the spectral features in the red to early-NIR spectral range of the optically active substances in the water body either using Level-2 or Level-1 data, without ambiguities caused by other processes. However, it is known that the overlap of chlorophyll and water absorption together with scattering can also produce a reflectance peak around 700 nm. One open question is the degree of ambiguity between the fluorescence peak as such and the peak resulting as a superposition of chlorophyll absorption, scattering and water absorption.
- The algorithm as it is assumes a fixed position of the fluorescence peak. In literature the hypothesis of a changing position with the phytoplankton functional type and species exists Zhao et al. (2010). However experts of phytoplankton physiology are convinced of a pretty fixed position of the fluorescence peak (pers. communication Rüdiger Roettgers, Hemlhotz Zentrum Geesthacht).
- The algorithm assumes the fluorescence peak to be Gaussian, while from laboratory measurements (pers. communication Rüdiger Roettgers) it looks slightly double Gaussian (see figure 44)

## 8.2 Potential Improvements

Following the above mentioned assumptions there are the following potential improvements:

- The OLCI $\rho_w$-FPH should in future be based on an exactly normalized quantity or a BRDF correction should be applied on the product itself.
- The retrieval uncertainty with respect to spectral ambiguities can be quantified by a specifically designed RTM study and should result in a flag for scums and a warning for ambiguous situations.

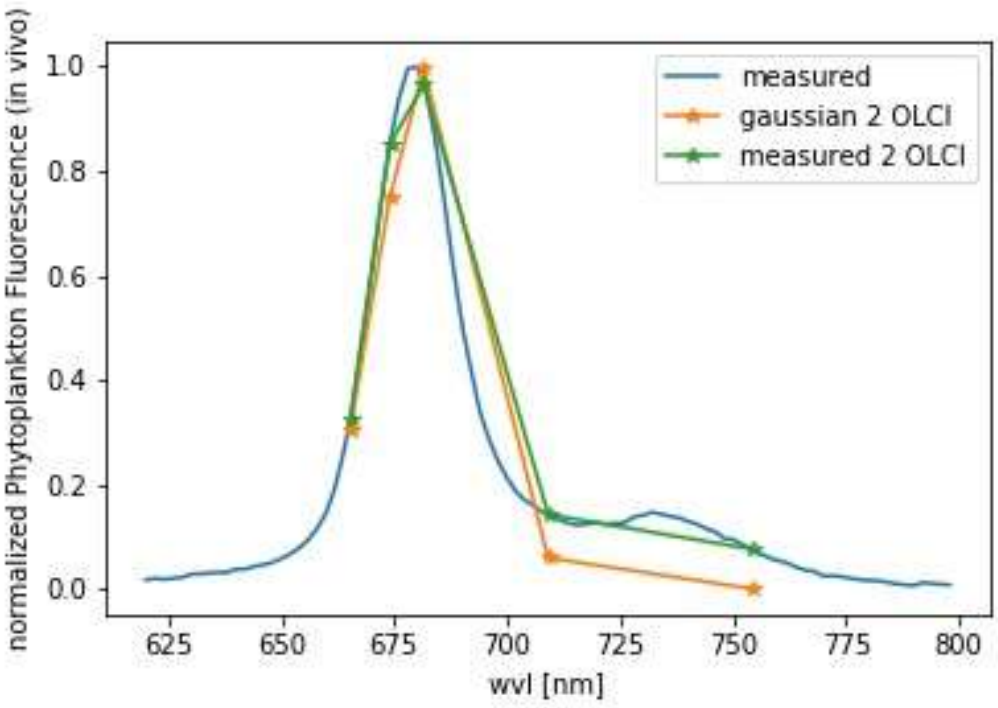


Figure 44: Measured normalized Phytoplankton Fluorescence (in vivo) (Rüdiger Röttgers), convoluted to OLCI srf, Gaussian convoluted to OLCI srf.

- Technically it is possible to include the position of the peak as retrieval parameter when more then 4 bands are available like with OLCI
- The replacement of the Gaussian function for fluorescence by the measured fluorescence spectral shape was tested and did not improve the fit.

# 9 Algorithm limitations and application recommendations

The sensitivity range of the algorithm is determined by the sensitivity of the measurements towards the fluorescence signal and the ability of algorithm to retrieve it. From our fluorescence to chlorophyll comparisons and in agreement with earlier assessments (see section 1.3), we estimate the sensitivity range of the processor to chlorophyll $> 1\,mg/m^3$ which corresponds to L-FPH $> 0\ mWm^{-2}sr^{-1}nm^{-1}$ and $\rho_w$-FPH $> 0.1$. This is based on the observation that below this threshold data can become noisy and L-FPH values become negative. This sensitivity threshold will also be subject to further investigations.

| Parameter | Chlorophyll | L-FPH | $\rho_w$-FPH |
|---|---|---|---|
| sensitivity threshold | $1\,mg/m^3$ | $0\ mWm^{-2}sr^{-1}nm^{-1}$ | 0.1 |

Table 6: Sensitivity thresholds for the output parameter of the OC-Fluo algorithm.

Additionally the conversion from FPH to chlorophyll (see Sect. 6) relies on a global

relationship and is therefore only a rough estimate due to reasons given in Sect. 4.1.

# 10 Potential Future Evolutions and Recommendations

To base the OLCI $\rho_w$-FPH on an exactly normalized quantity or to apply a BRDF correction on $\rho_w$-FPH is the most urgent topic since it would decrease the product uncertainty significantly. The quantification of retrieval uncertainties should be the second priority. For the moment the improvement by including the position of the fluorescence peak as retrieval parameter and the replacement of the Gaussian function for fluorescence by the measured fluorescence spectral shape is not very promising. For simplicity we recommend to keep the Gaussian instead of the measured fluorescence function.

## 10.1 BRDF correction for FPH

Before an operational availability of exactly normalized water-leaving reflectance from OLCI, a BRDF correction of the FPH should be aimed for. From RTM simulations $\rho_w$ and the resulting $\rho_w$-FPH can be calculated for any viewing geometry. The ratio of $\rho_w$-FPH at the specific viewing geometry from the measurement to $\rho_w$-FPH associated with the same water body but based on $\theta_v^N$ gives a BRDF correction factor for the retrieved $\rho_w$-FPH in order to get a normalized $\rho_w$-FPH. We recommend to implement this in the retrieval procedure.

## 10.2 Flag for scums and warning for ambiguous situations

The signal which is emerging the water body can be ambiguous with respect to fluorescence and other water constituents. The combined phytoplankton and water absorption spectra, with the confluence of the decreasing phytoplankton absorption and the increasing absorption of water with wavelength results in a local absorption minimum. This absorption minimum leads to the maximum in the reflectance spectra which are inversely related to the total absorption. From validation against in-situ chlorophyll we cannot decide if we are detecting pure fluorescence (inelastic) or the combination of both, fluorescence and the absorption/scattering (elastic) peak because the relation between chlorophyll concentration and fluorescence is also depending on fluorescence efficiency and layering of the phytoplankton (see Figure 45).

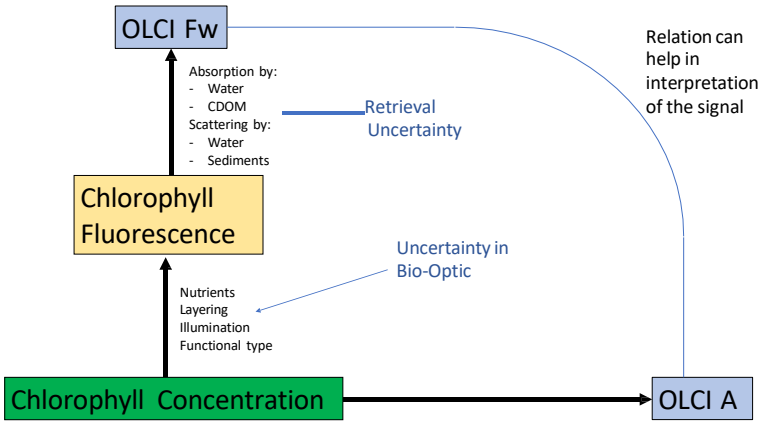


Figure 45: Relation between chlorophyll concentration, fluorescence and absorption

The retrieval uncertainty can be quantified through radiative transfer studies with the fol-

lowing strategy (see also Figure 8). A global range of chlorophyll concentrations is input to the bio-optical model (0-300 mg/m$^3$). In contrast to the study performed during the project, chlorophyll fluorescence, absorption and scattering should not be coupled, but varied independently as input parameter. This should be done in each case at 10 logarithmically distributed sampling points with fixed chlorophyll concentration. The relation between chlorophyll absorption and fluorescence is the fluorescence efficiency, which has been set for this study in MOMO at 0.03.

In the first part of the study the fluorescence efficiency should be varied over a broad range (e.g. 0.01 - 0.3), so that with fixed absorption and scattering, there is a varying fluorescence signal. In the second part of the study scattering should be varied, while the fluorescence efficiency is fixed. The RTM MOMO simulations should be performed in the range from 600-800 nm with 1 nm sampling. From the output remote sensing reflectances are calculated and convoluted using OLCI spectral response functions. The OC-Fluo algorithm is applied to those spectra and the resulting FPH is correlated to the input parameter with the attempt to also find correlations to A, S and O. This sensitivity study should result in a recommendation for flags/warnings to be raised when the product is uncertain to a high extend. It can also be used to include bio-optical uncertainties in the uncertainty estimation of the product.

## 10.3 Validation of A

The OC-Fluo algorithm results in 4 retrieval parameters. Offset (O), Slope (S), Absorption coefficient (A) and Fluorescence coefficient (FPH). The project period allowed the thorough investigation of FPH only. However, A seems to be a good proxy for phytoplankton biomass, as it is valid for the maximum absorption in the blue spectral range. The retrieval parameter A should be validated against chlorophyll in a very similar manner like FPH. This means the validation of A against OLCI OC4me and NN and against insitu chlorophyll concentration from the MDB. Chlorophyll absorption is a good proxy for phytoplankton biomass.

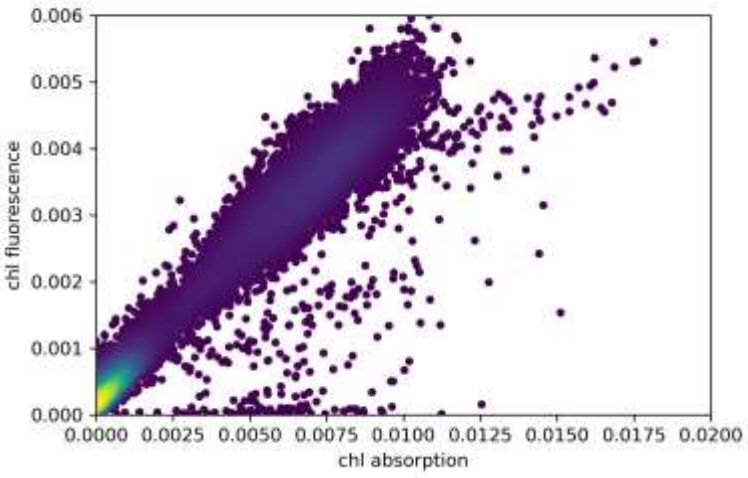


Figure 46: Correlation between chlorophyll fluorescence and absorption

## 10.4 Analysis of the relation of L-FPH or $\rho_w$-FPH and A for information on layering, phytoplankton species, and physiological states

Since both retrieval parameters, A and FPH are signals originating from chlorophyll, the combination of both can give new insights into the biology and the layering of the phytoplankton (see Figure 45). As introduced above, A could be a correction on $F_w$ with respect to layering. Fig. 46 shows the strong correlation of A and FPH in the Barents Sea. The retrieval parameter A, which is evaluated in the red, is affected in the same way by the specific layering of the phytoplankton as the parameter FPH due to the radiative transfer in the water. But it is not affected in the same way, or not as intensively by phytoplankton species, physiological state or photoinhibition.

# References

M. Babin, A. Morel, and B. Gentili. Remote sensing of sea surface Sun-induced chlorophyll fluorescence: consequences of natural variations in the optical characteristics of phytoplankton and the quantum yield of chlorophyll a fluorescence. *International Journal of Remote Sensing*, 17(12):2417-2448, 8 1996. ISSN 0143-1161. doi: 10.1080/01431169608948781. URL https://www.tandfonline.com/doi/full/10.1080/01431169608948781.

M. J. Behrenfeld, T. K. Westberry, E. S. Boss, R. T. O'Malley, D. A. Siegel, J. D. Wiggert, B. A. Franz, C. R. McClain, G. C. Feldman, S. C. Doney, J. K. Moore, G. Dall'Olmo, A. J. Milligan, I. Lima, and N. Mahowald. Satellite-detected fluorescence reveals global physiology of ocean phytoplankton. *Biogeosciences*, 6(5):779-794, 5 2009. ISSN 1726-4189. doi: 10.5194/bg-6-779-2009. URL http://www.biogeosciences.net/6/779/2009/.

C. E. Binding, T. A. Greenberg, J. H. Jerome, R. P. Bukata, and G. Letourneau. An assessment of MERIS algal products during an intense bloom in Lake of the Woods. *Journal of Plankton Research*, 33(5):793-806, 5 2011. ISSN 0142-7873. doi: 10.1093/plankt/fbq133. URL https://academic.oup.com/plankt/article-lookup/doi/10.1093/plankt/fbq133.

G. A. Borstad, H. R. Edel, J. Gower, and A. B. Hollinger. Analysis of test and flight data from the Fluorescence Line Imager. Technical report, 1987. URL http://publications.gc.ca/site/eng/9.816405/publication.html.

L. Bourg, E. Vincent, and I. Muguet. OLCI Level 2 Algorithm Theoretical Basis Document, 2010. URL https://sentinel.esa.int/documents/247904/349589/OLCI_L2_ATBD_Instrumental_Correction.pdf.

A. Bricaud, M. Babin, H. Claustre, J. Ras, and F. Tièche. Light absorption properties and absorption budget of Southeast Pacific waters. *Journal of Geophysical Research: Oceans*, 115(8):1-19, 2010. ISSN 21699291. doi: 10.1029/2009JC005517.

C. Brockmann, R. Doerffer, P. Marco, K. Stelzer, S. Embacher, and A. Ruescas. Evolution Of The C2RCC Neural Network For Sentinel 2 and 3 For The Retrieval of Ocean. *Proc. 'Living Planet Symposium 2016', Prague, Czech Republic, 9–13 May 2016 (ESA SP-740, August 2016)*, 2016(August): 9-13, 2016.

Craig Donlon. estec Sentinel-3 Mission Requirements Traceability Document (MRTD) - PDF. Technical report, European Space Research and Technology Centre, 2011. URL http://docplayer.net/18739996-Estec-sentinel-3-mission-requirements-traceability-document-mrtd.html.

C. Donlon, B. Berruti, A. Buongiorno, M.-H. Ferreira, P. Féménias, J. Frerick, P. Goryl, U. Klein, H. Laur, C. Mavrocordatos, J. Nieke, H. Rebhan, B. Seitz, J. Stroede, and R. Sciarra. The Global Monitoring for Environment and Security (GMES) Sentinel-3 mission. *Remote Sensing of Environment*, 120:37-57, 5 2012. ISSN 00344257. doi: 10.1016/j.rse.2011.07.024. URL https://linkinghub.elsevier.com/retrieve/pii/S0034425712000685.

M. Drinkwater and H. Rebhan. Sentinel-3: Mission Requirements Document. Technical report, 2005. URL http://scholar.google.com/scholar?hl=en&btnG=Search&q=intitle:

Sentinel-3:+Mission+Requirements+Document#0.

Z. K. Erickson, C. Frankenberg, D. R. Thompson, A. F. Thompson, and M. Gierach. Remote Sensing of Chlorophyll Fluorescence in the Ocean Using Imaging Spectrometry: Toward a Vertical Profile of Fluorescence. *Geophysical Research Letters*, 46(3):1571–1579, 2 2019. ISSN 0094-8276. doi: 10.1029/2018GL081273. URL https://onlinelibrary.wiley.com/doi/abs/10.1029/2018GL081273.

EUMETSAT. Recommendations for Sentinel-3 OLCI Ocean Colour product validations in comparison with in situ measurements – Matchup Protocols. pages 1–10, 2019.

Eumetsat Ocean Color In-situ Database. Ocean Colour In-Situ Database, 2019. URL https://ocdb.eumetsat.int/.

P. Falkowski and D. A. Kiefer. Chlorophyll a fluorescence in phytoplankton: relationship to photosynthesis and biomass. *Journal of Plankton Research*, 7(5):715–731, 1985. ISSN 0142-7873. doi: 10.1093/plankt/7.5.715. URL https://academic.oup.com/plankt/article-lookup/doi/10.1093/plankt/7.5.715.

G. C. Feldman. NASA's OceanColor Web. URL oceancolor.gsfs.nasa.gov.

F. Fell and J. Fischer. Numerical simulation of the light field in the atmosphere-ocean system using the matrix-operator method. *Journal of Quantitative Spectroscopy and Radiative Transfer*, 69(3):351–388, 2001. ISSN 00224073. doi: 10.1016/S0022-4073(00)00089-3.

J. Fischer and U. Kronfeld. Sun-stimulated chlorophyll fluorescence 1: Influence of oceanic properties. *International Journal of Remote Sensing*, 11(12):2125–2147, 1990. ISSN 13665901. doi: 10.1080/01431169008955166.

J. Fischer, R. Preusker, and R. Lindstrot. Correction of the impact of the absorption of atmospheric gases – OLCI Level 2 Algorithm Theoretical Basis Document. pages 1–37, 2010.

H. Gons, M. Auer, S. E. R. S. o. Environment, and U. 2008. MERIS satellite chlorophyll mapping of oligotrophic and eutrophic waters in the Laurentian Great Lakes. *Elsevier*, 2008. URL https://www.sciencedirect.com/science/article/pii/S0034425708002083.

H. R. Gordon and K. J. Voss. MODIS Normalized Water-leaving Radiance Algorithm Theoretical Basis Document (MOD 18). Technical Report Mod 18, 1999.

J. Gower. A simpler picture of satellite chlorophyll fluorescence. *Remote Sensing Letters*, 5 (6):583–589, 6 2014. ISSN 2150-704X. doi: 10.1080/2150704X.2014.940630. URL http://www.tandfonline.com/doi/abs/10.1080/2150704X.2014.940630.

J. Gower and S. King. Validation of chlorophyll fluorescence derived from MERIS on the west coast of Canada. *International Journal of Remote Sensing*, 28(3–4):625–635, 2007a. ISSN 01431161. doi: 10.1080/01431160600821010.

J. Gower and S. King. Validation of chlorophyll fluorescence derived from MERIS on the west coast of Canada. *International Journal of Remote Sensing*, 28(3–4):625–635, 2 2007b. ISSN 0143-1161. doi: 10.1080/01431160600821010. URL https://www.tandfonline.com/doi/full/10.1080/01431160600821010.

J. Gower and S. King. Use of satellite images of chlorophyll fluorescence to monitor the spring bloom in coastal waters. *International Journal of Remote Sensing*, 33(23):7469–7481, 12 2012. ISSN 0143-1161. doi: 10.1080/01431161.2012.685979. URL https://www.tandfonline.com/doi/full/10.1080/01431161.2012.685979.

A. L. I. f. B. S. Hansen. podcampus | Phytoplankton analysis off the coast of Namibia, 2014. URL https://www.podcampus.de/nodes/QVKNA.

F. E. Hoge, P. E. Lyon, R. N. Swift, J. K. Yungel, M. R. Abbott, R. M. Letelier, and W. E. Esaias. Validation of Terra-MODIS phytoplankton chlorophyll fluorescence line height I Initial airborne

lidar results. *Applied Optics*, 42(15):2767, 5 2003. ISSN 0003-6935. doi: 10.1364/AO.42.002767. URL https://www.osapublishing.org/abstract.cfm?URI=ao-42-15-2767.

A. Hollstein and J. Fischer. Radiative transfer solutions for coupled atmosphere ocean systems using the matrix operator technique. *Journal of Quantitative Spectroscopy and Radiative Transfer*, 113(7):536–548, 2012. ISSN 00224073. doi: 10.1016/j.jqsrt.2012.01.010.

C. Hu, F. E. Muller-Karger, C. J. Taylor, K. L. Carder, C. Kelble, E. Johns, and C. A. Heil. Red tide detection and tracing using MODIS fluorescence data: A regional example in SW Florida coastal waters. *Remote Sensing of Environment*, 97(3):311–321, 8 2005. ISSN 0034-4257. doi: 10.1016/J.RSE.2005.05.013. URL https://www.sciencedirect.com/science/article/abs/pii/S0034425705001598.

Y. Huot, C. A. Brown, and J. J. Cullen. New algorithms for MODIS sun-induced chlorophyll fluorescence and a comparison with present data products. *Limnology and Oceanography: Methods*, 3(2):108–130, 2 2005. ISSN 15415856. doi: 10.4319/lom.2005.3.108. URL http://doi.wiley.com/10.4319/lom.2005.3.108.

I. Ioannou, J. Zhou, A. Gilerson, B. Gross, F. Moshary, and S. Ahmed. New algorithm for MODIS chlorophyll fluorescence height retrieval: performance and comparison with the current product. page 747309, 9 2009. doi: 10.1117/12.830630. URL http://proceedings.spiedigitallibrary.org/proceeding.aspx?doi=10.1117/12.830630.

S. Jeffrey and G. Humphrey. New spectrophotometric equations for determining chlorophylls a, b, c1 and c2 in higher plants, algae and natural phytoplankton. *Biochemie und Physiologie der Pflanzen*, 167(2):191–194, 1975. ISSN 00153796. doi: 10.1016/s0015-3796(17)30778-3. URL http://dx.doi.org/10.1016/S0015-3796(17)30778-3.

D. A. Kiefer. Fluorescence properties of natural phytoplankton populations. *Marine Biology*, 22(3):263–269, 1973. ISSN 0025-3162. doi: 10.1007/BF00389180. URL http://link.springer.com/10.1007/BF00389180.

L. Kritten and R. Preusker. OLCI's smile on remote sensing reflectances of water and a simple retrieval of chlorophyll absorption and fluorescence for TOA radiances. Number 2, pages 1–6, 2017.

R. Letelier. An analysis of chlorophyll fluorescence algorithms for the moderate resolution imaging spectrometer (MODIS). *Remote Sensing of Environment*, 58(2):215–223, 11 1996. ISSN 00344257. doi: 10.1016/S0034-4257(96)00073-9. URL http://linkinghub.elsevier.com/retrieve/pii/S0034425796000739.

H. Lin, F. I. Kuzminov, J. Park, S. Lee, P. G. Falkowski, and M. Y. Gorbunov. Phytoplankton. The fate of photons absorbed by phytoplankton in the global ocean. *Science (New York, N.Y.)*, 351(6270):264–7, 1 2016. ISSN 1095-9203. doi: 10.1126/science.aab2213. URL http://www.ncbi.nlm.nih.gov/pubmed/26743625.

C. Mazeran, C. B. Brockmann, K. Ruddick, K. Voss, and F. Zagolski. Requirements for Copernicus Ocean Colour Vicarious Calibration Infrastructure. Number July, 2017.

A. Morel, B. Gentili, H. Claustre, M. Babin, A. Bricaud, J. Ras, and F. Tièche. Optical properties of the "clearest" natural waters. *Limnology and Oceanography*, 52(1):217–229, 2007. ISSN 00243590. doi: 10.4319/lo.2007.52.1.0217.

M. J. Moreno-Madriñán and A. M. Fischer. Performance of the MODIS FLH algorithm in estuarine waters: a multi-year (2003–2010) analysis from Tampa Bay, Florida (USA). *International Journal of Remote Sensing*, 34(19):6467–6483, 10 2013. ISSN 0143-1161. doi: 10.1080/01431161.2013.

804227. URL https://www.tandfonline.com/doi/full/10.1080/01431161.2013.804227.

NASA. Phytoplankton Bloom off Namibia, 2017. URL https://www.nasa.gov/multimedia/imagegallery/image_feature_975.html.

R. A. Neville and J. F. R. Gower. Passive remote sensing of phytoplankton via chlorophyll α fluorescence. *Journal of Geophysical Research*, 82(24):3487–3493, 8 2008. ISSN 01480227. doi: 10.1029/jc082i024p03487. URL http://doi.wiley.com/10.1029/JC082i024p03487.

D. Odermatt, A. Gitelson, V. E. Brando, and M. Schaepman. Review of constituent retrieval in optically deep and complex waters from satellite imagery. *Remote Sensing of Environment*, 118:116–126, 3 2012. ISSN 00344257. doi: 10.1016/j.rse.2011.11.013. URL https://www.sciencedirect.com/science/article/pii/S0034425711004081.

T. Petzold. Volume Scattering Functions for Selected Ocean Waters. *Scripps Inst. Oceanogr.*, (3): 72–78, 1972. ISSN 1936-900X. doi: 10.5811/westjem.2013.7.18472. URL http://oai.dtic.mil/oai/oai?verb=getRecord&metadataPrefix=html&identifier=AD0753474.

C. D. Rodgers. *Inverse Methods for Atmospheric Sounding: Theory and Practice.* World Scientific., 2000.

R. Röttgers, R. Doerffer, D. Mckee, and W. Schönfeld. Pure water spectral absorption, scattering, and real part of refractive index model Algorithm Technical Basis Document – Draft. Technical report, 2010.

M. H. Schlüter. *Investigating environmental changes in thesouthern North Sea: a combined statisticalassessment of climatic and biogeochemicallong–term time series*. PhD thesis, Hamburg, 2010.

P. J. Werdell, S. Bailey, G. Fargion, C. Pietras, K. Knobelspiesse, G. Feidman, and C. Mcclain. Unique data repository facilitates ocean color satellite validation. *Eos*, 84(38):2002–2004, 2003. ISSN 00963941. doi: 10.1029/2003EO380001.

A. Wolanin, V. Rozanov, T. Dinter, S. Noël, M. Vountas, J. Burrows, and A. Bracher. Global retrieval of marine and terrestrial chlorophyll fluorescence at its red peak using hyperspectral top of atmosphere radiance measurements: Feasibility study and first results. *Remote Sensing of Environment*, 166:243–261, 9 2015. ISSN 0034-4257. doi: 10.1016/J.RSE.2015.05.018. URL https://www.sciencedirect.com/science/article/pii/S0034425715300183.

X. G. Xing, D. Z. Zhao, Y. G. Liu, J. H. Yang, P. Xiu, and L. Wang. An overview of remote sensing of chlorophyll fluorescence. *Ocean Science Journal*, 42(1):49–59, 2007. ISSN 17385261. doi: 10.1007/BF03020910.

X. Zhang and L. Hu. Scattering by pure seawater at high salinity. *Optics Express*, 17(15):12685, 2009. ISSN 1094-4087. doi: 10.1364/OE.17.012685. URLhttps://www.osapublishing.org/oe/abstract.cfm?uri=oe-17-15-12685.

D. Zhao, X. Xing, Y. Liu, J. Yang, and L. Wang. The relation of chlorophyll-a concentration with the reflectance peak near 700 nm in algae- dominated waters and sensitivity of fluorescence algorithms for detecting algal bloom. 1161, 2010. doi: 10.1080/01431160902882512.

J. Zhou, A. Gilerson, I. Ioannou, S. Hlaing, J. Schalles, B. Gross, F. Moshary, and S. Ahmed. Retrieving quantum yield of sun-induced chlorophyll fluorescence near surface from hyperspectral in-situ measurement in productive water. *Optics Express*, 16(22):17468, 2008. ISSN 1094-4087. doi: 10.1364/oe.16.017468.